Investigating the influence of transition metal substitution in lithium argyrodites on structure, transport and solid-state battery performance

Johannes Hartel,¹ Ananya Banik,² Md Yusuf Ali,³ Bianca Helm,⁴ Kyra Strotmann,¹ Vasiliki Faka,¹ Oliver Maus,^{1,5} Cheng Li,⁶ Hartmut Wiggers,^{3,7} Wolfgang G. Zeier^{1,8*}

¹Institute of Inorganic and Analytical Chemistry, University of Münster, Corrensstrasse 28/30, 48149 Münster, Germany

²Research Institute for Sustainable Energy (RISE), TCG Centre for Research and Education in Science and Technology (TCG-CREST), 700091 Kolkata, India

³Institute for Energy and Materials Process-Reactive Fluids, University of Duisburg-Essen, Carl-Benz-Strasse 199, 47057 Duisburg, Germany

⁴Bavarian Center for Battery Technology (BayBatt), University of Bayreuth,
Universitätsstrasse 30, 95447 Bayreuth, Germany

⁵International Graduate School BACCARA, Wilhelm-Schickard-Straße 8, 48149 Münster, Germany

⁶Neutron Scattering Division, Oak Ridge National Laboratory (ORNL), Oak Ridge, Tennessee 37831-6473, United States

⁷CENIDE, Center for Nanointegration, University of Duisburg-Essen, Carl-Benz-Strasse 199, 47057 Duisburg, Germany

⁸Institute of Energy Materials and Devices (IMD), IMD-4: Helmholtz-Institut Münster, Forschungszentrum Jülich, 48149 Münster, Germany.

*wzeier@uni-muenster.de

Abstract

Lithium argyrodites have gained significant attention as candidates for solid electrolytes in solid-state batteries due to their superior ionic conductivities and favorable mechanical properties. However, during charging, oxidative decomposition reactions occur at the interface between the solid electrolyte and cathode active material which impede cell performance. In this study, transition metal substitution of the solid electrolyte is investigated with the intention to tune the composition of the cathode electrolyte interphase (CEI) and thereby improve the cycling performance. Hence, the Li_{5.5-2x}Zn_xPS_{4.5}Cl_{1.5} ($0 \le x \le 0.15$) and $\text{Li}_{6-2x}\text{Zn}_x\text{PS}_5\text{Br}$ (0 $\leq x \leq$ 0.15) substitution series are investigated to elucidate how substitution affects structure, Li+ transport and the performance of the materials as catholytes in solidstate batteries. Co-refinement of the neutron and X-ray powder diffraction data unveils the occupation of Li⁺ positions by Zn²⁺. This leads to blocking of Li⁺ transport pathways within the Li⁺ cages causing a decrease of ionic conductivities along with increasing activation energies for Li⁺ transport. By using a combination of cycling experiments, impedance spectroscopy and X-ray photoelectron spectroscopy, the composition of the CEI and the state-of-charge dependence of the CEI growth when using Li_{5.5-2x}Zn_xPS_{4.5}Cl_{1.5} NCM-83 composites was investigated in half-cells, revealing that Zn²⁺ substitution leads to faster decomposition kinetics and affects the CEI composition. Overall, this work explores the influence of Li⁺ substitution by Zn²⁺ on structure and transport in lithium argyrodites and the potential of transition metal substitutions as means to tune the kinetics of CEI growth, the CEI composition and thereby cell performance.

1. Introduction

Solid-state batteries are a promising alternative to conventional lithium-ion batteries containing liquid electrolytes, potentially enabling higher safety and improved performance.¹ Successful implementation of a lithium metal^{2,3} or high-capacity silicon anode^{2,3} in solid-state batteries may additionally allow the construction of solid-state batteries with even higher energy and power densities than state-of-the-art lithium-ion batteries.

Nevertheless, solid-state batteries suffer from low effective ionic conductivities in composite electrodes due to the presence of voids and grain boundaries, and require intimate particle-particle contact between the solid electrolyte and the active material.^{4,5} Thus, ultrafast Li⁺ conductors with ionic conductivities of 10 mS·cm⁻¹ or higher are needed as solid electrolytes in composite cathodes (catholytes) or in composite anodes (anolytes).^{6,7} In the last decades, a great variety of Li⁺ superionic solid electrolytes have been investigated including oxides, phosphates, halides and thiophosphates.⁸ Among these, lithium thiophosphates and in particular the class of lithium argyrodites Li₆PS₅X (X = CI, Br, I) stand out owing to their exceptionally high ionic conductivities and their structural tunability.^{9,10} Elemental substitutions, including iso- and aliovalent substitutions on the P(V) position, for example with Sb(V),¹¹ Ge(IV),^{12,13} Si(IV),¹⁴ or Sn(IV)¹⁴ or substitutions on the sulfide position e.g. by selenide^{15,16} have proven to be effective strategies to boost ionic conductivities of lithium argyrodites beyond 10 mS·cm⁻¹. Similarly, increasing the halide content in lithium argyrodites in Li_{6-x}PS_{5-x}Cl_{1+x}^{17,18}, Li_{6-x}PS_{5-x}Br_{1+x}¹⁹ and Li_{6-x}PSe_{5-x}Br_{1+x}¹⁵ or high entropy compositions such as Li_{6-x}PO₂₋₅Si_{0.25}Ge_{0.25}Sb_{0.25}Sl₅₋₂₅Ssi_{0.25}Sl₅₋₂₅Ssi_{0.25}Sl₅₋₂₅Ssi

At room temperature, lithium argyrodites Li_6PS_5X (X = Cl, Br, I) crystallize in the high-temperature cubic polymorph with space group $F\overline{4}3m$. The halide anions X^- provide a face-centered cubic sublattice (Wyckoff 4a), where every octahedral void is occupied by a (PS₄)³⁻ tetrahedron (P on Wyckoff 4b and S on Wyckoff 16e) and half of the tetrahedral voids are occupied by S²⁻ (Wyckoff 4d) as shown in Figure S1.²¹ There is X^-/S^2 - site-disorder for $X^- = \text{Cl}^-$ and Br⁻ due to the more similar ionic radii compared to S²⁻, while for $X^- = \text{I}^-$ the crystal structure is fully ordered in the unsubstituted material.²² There are five tetrahedral voids, that can potentially be occupied by Li⁺ (T1 to T5).²³ Depending on the composition and the degree of X^-/S^2 - site-disorder, the distribution of Li⁺ across these tetrahedral voids differs. In lithium argyrodites with no site-disorder such as Li₆PS₅I, the lithium-ions occupy only T5 and T5a

positions, forming defined cages around S^{2-} (Wyckoff 4d), not allowing for long-range Li⁺ transport.^{23,24} In contrast, for compositions with a significant degree of site-disorder including Li₆PS₅Cl, Li₆PS₅Br, and several other substitutions, the occupation of additional Li⁺ positions including T2, T4 and T3 has been observed. Occupancy on these positions opens up pathways for inter-cage Li⁺ diffusion leading to ionic conductivities greater than 1 mS·cm⁻¹ of these compounds.^{13,18,23,25} Furthermore, a high degree of site-disorder has been found to result in a larger mean distance of Li⁺ from the Wyckoff 4d position (R_{mean}) due to decreased Coulomb attraction, leading to a better interconnection of the Li⁺ substructure and hence facilitating Li⁺ transport.^{13,18,26,27} The X^-/S^{2-} site-disorder and thereby the lithium-ion distribution of lithium argyrodites can not only be tuned by elemental substitutions, but also by the optimization of the synthesis protocol.^{27,28}

Due to their high ionic conductivities, lithium argyrodites are frequently applied as catholytes in lithium nickel cobalt manganese oxide (NCM) based composite cathodes in solid-state batteries. Despite high obtainable capacities in the first cycles, (electro-)chemical decomposition upon charging leads to formation of a cathode electrolyte interface (CEI) and thereby continuous capacity fading and high cell resistances. At potentials below ~3.6 V vs In/InLi (4.2 V vs Li⁺/Li), electrochemical decomposition dominates, leading to delithiation and the formation of polysulfides and anionic phosphorus and sulfur-containing frameworks. At higher potentials above ~3.6 V vs In/InLi (4.2 V vs Li⁺/Li) solid and gaseous oxygenated sulfur and phosphorus species such as sulfites and sulfates, phosphates and SO₂ are formed. The oxygen depletion at the NCM surface further leads to the conversion from a layered to a rock salt-like structure, whereas the gas evolution and volume changes due to (electro-)chemical reactions increases the porosity of the CEI. The oxygen depletion is increases the porosity of the CEI.

To prevent the (electro-)chemical decomposition when utilizing lithium argyrodites as catholytes in NCM-based composite cathodes, coatings are applied on NCM particles to mitigate decomposition reactions.³⁷ Even though coatings such as LiNbO₃³⁸ or Al₂O₃³⁹ have been quite successful, delamination or cracking of the coating layer, due to volumetric changes of NCM during cycling and interdiffusion, is observed.³⁷ Hence, coating strategies successfully slow down (electro-)chemical degradation but cannot fully eliminate it, calling for additional protection concepts.

Herein, CEI design by substitution of the catholyte is explored as a potential strategy to mitigate the detrimental effects of (electro-)chemical decomposition by formation of a CEI with more favorable properties for stable long-term cycling (Figure 1). These include a high ionic conductivity and low electronic conductivity³⁷, a high oxidative stability³², and a decreased porosity. ⁴⁰ The composition of lithium argyrodites has been shown to affect the CEI composition and the kinetics of its formation in NCM-based composite cathodes, which significantly impacts battery performance. For instance, Zuo *et al.* have reported that the use of Li_{5.5}PS_{4.5}Cl_{1.5} instead of Li₆PS₅Cl as catholyte leads to formation of more polysulfides and gaseous decomposition products and less solid oxygenated sulfur and phosphorus compounds, which is more favorable for cell performance. ⁴¹ Lin *et al.* have found that the use of Li_{6.5}[P_{0.25}Si_{0.25}Ge_{0.25}Sb_{0.25}]S₅I catholyte in NCM-based solid-state batteries leads to fast capacity fading due to formation of oxidated and oxygenated decomposition products based on Si, Ge and Sb, showing that substitutions incorporating these elements are detrimental for the long-term solid-state battery performance even though they lead to faster Li⁺ transport of the solid electrolytes. ²⁰

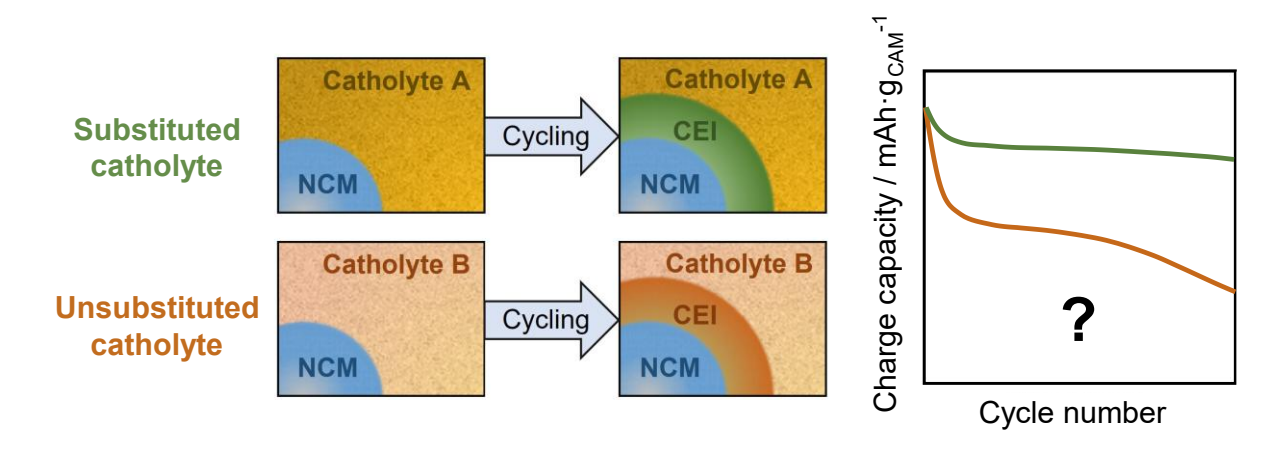


Figure 1: Illustration of a potential CEI design hypothesis. Using a substituted solid electrolyte as catholyte leads to the formation of a CEI with a different composition which may have more favorable properties such as higher ionic conductivity, lower electronic conductivity, higher oxidative stability or decreased porosity to enable stable cycling performance.

Encouraged by the works of Zuo and Lin *et al.* that indicate a strong correlation between the composition of the catholyte, CEI composition and cell performance, the Li_{5.5-2x}Zn_xPS_{4.5}Cl_{1.5} ($0 \le x \le 0.15$) and Li_{6-2x}Zn_xPS₅Br ($0 \le x \le 0.15$) substitution series are investigated to elucidate how transition metal substitution with Zn²⁺ affects the performance of the materials as catholytes in solid-state batteries, and further the kinetics of CEI formation and the

composition of the CEI. While transition metal substitution on Li⁺ positions has already been reported for $Li_{6-2x}Zn_xPS_{5-x}O_xBr^{42}$, $Li_{7-2x}Fe_xPS_6^{43}$ and $Li_{6-2x}Cu_xPS_{5-x}Br_{1+x}^{44}$, the effects on the Li^+ substructure and the structure-transport relationship of the material and further have not been investigated. Additionally, only the impact of Zn²⁺ substitution on the application in conjunction with the lithium metal anode has been tested, while the impact on the performance of composite cathodes incorporating such electrolytes as catholyte, are not fully understood yet. Substitution of Zn²⁺ appears promising, since ZnO additives have been shown to enable improved cycling performance of Li₆PS₅Cl|NCM composite cathodes by mitigating oxidative decomposition.⁴⁵ Potential decomposition products such as ZnS are known to absorb SO₂, similarly to ZnO and may thereby mitigate decomposition.⁴⁶ Furthermore, Zn²⁺ is not expected to be redox active within the operating voltage range of NCM-based solid-state batteries in contrast to other transition metals with appropriate ionic radii such as Fe²⁺.⁴⁷ Therefore, a higher structural stability of Zn²⁺-based solid electrolytes during SSB cycling compared to SEs incorporating redox-active transition metal species is expected. As compared to an additive, the substitution approach enables an even distribution of Zn²⁺ within the solid electrolyte and thereby enables to omit the mixing step of solid electrolyte and additive.

In this work, blocking of intra-cage transport pathways by introduction of Zn²⁺ on T5 positions within the Li⁺ cages is revealed as a cause for decreasing ionic conductivities and increasing activation energies upon substitution by co-refinement of neutron powder diffraction and X-ray powder diffraction data. Additionally, cycling of half-cells unveils that application of the Zn²⁺ substituted argyrodites as catholytes leads to lower charge capacities and worse capacity retention. Using impedance spectroscopy, faster kinetics of CEI formation and higher resistance due to the CEI are revealed as potential causes for the lower charge capacities, when using Zn²⁺ substituted argyrodites as catholytes. Interestingly, while the kinetics of CEI formation mostly depends on the cutoff potential, they are found to be slightly faster for Zn²⁺ substituted argyrodites, irrespective of the cutoff potential. Analyses of cycled half-cells by X-ray photoelectron spectroscopy confirm that the amount of degradation products increases and the CEI composition changes at higher cutoff potentials, and further corroborates that Zn²⁺ substitution affects the degradation behavior of argyrodites.

Overall, this work explores the concept of CEI design by substitution of catholytes and extends the understanding of how aliovalent substitutions on lithium-ion positions affect structure and transport of lithium argyrodites. In turn, by adding transition metals into the argyrodites, this

work explores how much the performance of these materials as catholytes in solid-state batteries is affected.

2. Experimental Section

Synthesis. The syntheses of the Li_{5.5-2x}Zn_xPS_{4.5}Cl_{1.5} and Li_{6-2x}Zn_xPS₅Br substitution series ($0 \le x$ \leq 0.15) were performed in a glovebox under argon atmosphere (H₂O < 0.5 ppm, O₂ < 0.5 ppm). Lithium sulfide (Li₂S, Alfa-Aesar, 99.9%), zinc sulfide (ZnS, Merck, 99.99%), phosphorus pentasulfide (P₄S₁₀, Merck, 99%) and lithium chloride (LiCl, Alfa-Aesar, 99%) were mixed in stochiometric ratios to obtain Li_{5.5-2x}Zn_xPS_{4.5}Cl_{1.5}. Accordingly, lithium sulfide (Li₂S, Alfa-Aesar, 99.9%), zinc sulfide (ZnS, Merck, 99.99%), phosphorus pentasulfide (P_4S_{10} , Merck, 99%) and lithium bromide (LiBr, ultradry, Alfa-Aesar, 99.99%) were mixed in stochiometric ratio to obtain Li_{6-2x}Zn_xPS₅Br. The mixed precursors were manually ground in an agate mortar for 15 min and manually pressed into pellets before being filled into carbon coated quartz ampoules (length ~ 10-12 cm, diameter = 10 mm), which were previously dried at 800 °C under dynamic vacuum (p < 8 mbar) for 2 h. After sealing the ampoules under vacuum, they were transferred into a tube furnace. All Li_{5.5-2x}Zn_xPS_{4.5}Cl_{1.5} compositions were heated to 450 °C at a heating rate of 100 °C·h⁻¹ and annealed for 3 days followed by stopping the power supply of the oven and leaving the sample inside (natural cooling). The annealed pellets were hand ground for 15 min and then again pressed into pellets and sealed under vacuum in similarly pre-heated carbon coated quartz ampoules. Subsequently, the ampoules were again heated to 450 °C at a heating rate of 100 °C·h⁻¹ and annealed for 3 days. The Li_{6-2x}Zn_xPS₅Br were heated to 550 °C at a heating rate of 100 °C·h⁻¹ and annealed for 14 days, followed by quenching in liquid nitrogen to obtain a higher ionic conductivity than in the case of natural cooling (vide infra). All obtained pellets of the final reaction products were hand ground for further characterization and kept in the glovebox to avoid contact with moisture or oxygen.

Neutron powder diffraction. All neutron powder diffraction data of the $Li_{5.5-2x}Zn_xPS_{4.5}Cl_{1.5}$ and $Li_{6-2x}Zn_xPS_5Br$ ($0 \le x \le 0.15$) compositions were collected at the Oak Ridge spallation neutron source (SNS, Oak Ridge National Laboratory) at the POWGEN Time-Of-Flight diffractometer (BL-11A beamline) employing the PAC automatic sample changer. Roughly 2.5 g of samples were placed into cylindrical vanadium cans with a diameter of 8 mm and sealed under inert

atmosphere using a copper gasket. For each diffractogram, data were collected at 298 K for 2 h at a center wavelength of 1.5 Å in high-resolution mode.

Powder X-ray diffraction. Because of their air-sensitivity, all samples were measured in sealed borosilicate glass capillaries (Hilgenberg, 0.5 mm diameter). X-ray diffraction measurements were performed at room temperature on a STOE Stadi P diffractometer in Debye-Scherrer geometry using Mo-K_α radiation with a wavelength of 0.7093 Å, a curved Ge(111) monochromator and two Mythen 2k detectors. Diffraction experiments have been conducted in a Q range of 0.62 Å⁻¹ to 8.15 Å⁻¹, employing a 2 θ step-size of 0.1° and measuring for 20 s per step.

Rietveld analysis. TOPAS-Academic V6 software package⁴⁸ was used to carry out the Rietveld refinements on X-ray diffraction and absorption-corrected neutron powder diffraction data for all samples. The powder neutron and X-ray diffraction data for each composition were corefined as identical sample batches were used for data collection. The default weighting scheme of TOPAS Academic V6 software package was used for the co-refinement, which applies inverse variance weighting for both the neutron and X-ray diffraction data. This results in minimization of the overall chi-squared value, which equals the sum of the weighted residuals for the neutron and X-ray diffraction dataset. For the Li_{5.5-2x}Zn_xPS_{4.5}Cl_{1.5} and Li_{6-2x}Zn_xPS₅Br substitution series the structural models obtained from neutron refinements of Li_{5.5}PS_{4.5}Cl_{1.5} and Li₆PS₅Br by Gautam et al. ^{18,27} were used as starting models. To fit the peak shape, Pseudo-Voigt and GSAS back-to-back exponential functions were used for the neutron diffraction patterns and modified Thompson-Cox-Hastings pseudo-Voigt functions were applied to the X-ray diffraction patterns. The fit quality was assessed based on visual inspection and indicators including the goodness of fit (GOF) and R_{wp} . To achieve a suitable profile fit relevant parameters were refined in the following order: (1) Scale factor, (2) background fit using a Chebychev polynomial of 11th order, (3) lattice parameter and (4) peak shape. Once a good profile fit was achieved, the (5) isotropic thermal displacements parameters, (6) fractional atomic coordinates and (7) occupancies of the anionic framework were refined. Next, Li⁺ positions including T1-T5 and T5a were probed, using coordinates of these positions reported by Minafra et al.23 When unphysical values for displacement parameters ($B_{eq} < 0 \text{ Å}^2 \text{ or } B_{eq} > 6 \text{ Å}^2$) or negative occupancies were found, the sites were excluded from the refinement model. For all Li⁺ positions, the same displacement parameter was assumed due to their similar chemical environment, and this was needed for a stable refinement. Finally, all possible Zn²⁺ positions including T1-T5, T5a and the phosphorus position were probed, and similarly to the refinement of Li⁺ positions, sites were excluded from the refinement model when unphysical values for displacement parameters or negative occupancies occurred. Thereby, Zn²⁺ could only be found on T5 positions. The Li⁺, Cl⁻ and S²⁻ coordinates, occupancies, and displacement parameters with exception of the sulfide bound to phosphorus in the (PS₄)³⁻ unit were exclusively refined from the neutron powder diffraction data, while the Zn²⁺ occupancies were exclusively refined from X-ray powder diffraction data. For all remaining structural parameters both datasets were considered. The co-refined neutron and X-ray powder diffraction patterns, all constraints and the structural tables are given in the Supporting Information in Figure S2 and S3 and Tables S1-S10.

Potentiostatic electrochemical impedance spectroscopy. To determine the ionic conductivities, AC impedance was measured. First, approximately 300 mg of the assynthesized powders was pre-pelletized by hand before pressing isostatically at 413 MPa for 30 min, resulting in pellets with relative densities between 87% to 89% for all compositions. Then, approximately 100 nm thick gold layers were deposited on either side of the pellets using a Cressington Sputter Coater, applying a current of 30 mA and a sputtering time of 300 s under vacuum of 0.1 mbar. The sputtered pellets were then incorporated into pouch cells (~ 2 cm x 2 cm), attaching aluminum current collectors with Kapton® tape. For all compositions impedance spectra in the temperature range from 173 K to 298 K were measured using an Alpha-A impedance analyzer from Novocontrol Technologies applying an AC excitation voltage of 35 mV in a frequency range from 10 MHz to 50 mHz. The temperature was equilibrated for 1 h before each measurement to guarantee the targeted temperature has been reached. The RelaxIS 3 software package by rhd instruments was used for evaluation of the recorded impedance spectra. Using the Kramers-Kronig relations, the data quality was assessed to determine the frequency range for the fitting. The uncertainties for the determined ionic conductivities were calculated based on the fit and geometrical errors.

Assembly of solid-state batteries. For cycling experiments and to study the kinetics of cathode electrolyte interphase formation, half-cells with the composition $In/InLi|Li_{5.5}PS_{4.5}CI_{1.5}|NCM-83:Li_{5.5-2x}Zn_xPS_{4.5}CI_{1.5}$ (x=0,0.1) and with the composition $In/InLi|Li_6PS_5Br|NCM-83:Li_{6-2x}Zn_xPS_5Br$ (x=0,0.1) were assembled in a glovebox under argon atmosphere ($H_2O<0.5$ ppm, $O_2<0.5$ ppm) in press-cells.⁴⁹ Prior to its use $LiNi_{0.83}Co_{0.11}Mn_{0.06}O_2$ (NCM-83, MSE supplies) was dried under dynamic vacuum at 250 °C in a Büchi B-585 glass oven over

night. The cathode active material NCM-83 was mixed with the catholyte Li_{5.5-2x}Zn_xPS_{4.5}Cl_{1.5} (x = 0, 0.1) or $Li_{6-2x}Zn_xPS_5Br$ (x = 0, 0.1) in a weight ratio of 70:30 or 65:35, respectively. The higher catholyte weight fraction in the case of $Li_{6-2x}Zn_xPS_5Br$ (x = 0, 0.1) is required due to the higher density of this material, to maintain a constant volumetric ratio for all half-cells. The mixtures with a total mass of 100 mg were then soft milled for 15 min at 15 Hz using 5 ZrO₂ balls with a diameter of 5 mm each. To determine the porosity of the composite cathodes, 200 mg of the composites was pressed into pellets which were subsequently isostatically pressed at with 400 kN for 50 minutes. Subsequently, the half-cells were assembled by first adding 80 mg of Li_{5.5}PS_{4.5}Cl_{1.5} or Li₆PS₅Br as a separator and hand pressing. Next, 12 mg of cathode composite was evenly distributed across the surface of the separator and 3 t was applied uniaxially on the whole cell stack for 3 min, to achieve further densification of the materials. For preparation of the In/InLi anode, a lithium rod (abcr, 99.8%) was cut into 1-1.5 mg pieces and pressed into a foil, that was subsequently used together with an indium foil (chemPUR, 99.999%, 100 μm thickness, 9 mm diameter) to form the In/InLi alloy in-situ.⁵⁰ Next, the cells were tightly closed with a wrench and fixed in an aluminum frame applying a torque to keep the cell under ~60 MPa of stack pressure.

Electrochemical measurements. To allow for the In/InLi alloy to form, all half-cells were rested at OCV for 6 h before each electrochemical experiment. For all cycling experiments, the In/InLi|Li_{5.5}PS_{4.5}Cl_{1.5}|NCM-83:Li_{5.5-2x}Zn_xPS_{4.5}Cl_{1.5}|(x = 0, 0.1) and In/InLi|Li₆PS₅Br|NCM-83:Li_{6-2x}Zn_xPS₅Br|(x = 0, 0.1) half-cells were cycled between 2.0 V and 3.7 V vs In/InLi|(2.62 – 4.32 V vs Li⁺/Li) at 298 K, applying a C-rate of 0.1 C based on 200 mAh·g_{CAM}⁻¹ theoretical capacity of NCM-83. For the In/InLi|Li_{5.5}PS_{4.5}Cl_{1.5}|NCM-83:Li_{5.5-2x}Zn_xPS_{4.5}Cl_{1.5}|(x = 0, 0.1) half-cells, this corresponds to an areal capacity of $q_a = 2.14$ mAh·cm⁻² and a current density of j = 0.214 mA·cm⁻², while for In/InLi|Li₆PS₅Br|NCM-83:Li_{6-2x}Zn_xPS₅Br|(x = 0, 0.1) half-cells this corresponds to $q_a = 1.99$ mAh·cm⁻² and j = 0.199 mA·cm⁻². After each charge, the half-cells were rested for 1 h at OCV, followed by a PEIS measurement applying an AC voltage of 10 mV in a frequency range of 7 MHz to 10 mHz. The cell cycling and PEIS measurements were performed using a BioLogic VMP-300 potentiostat. Using the RelaxIS 3 software package by rhd instruments the data quality of the obtained spectra was assessed by the Kramers-Kronigs relations and the reliable frequency range was fit using a R-(RP)-(RP)-(RP)-P equivalent circuit, where R corresponds to a resistor and P to a constant phase element.

To investigate the growth kinetics of the CEI, $In/InLi|Li_{5.5}PS_{4.5}CI_{1.5}|NCM-83:Li_{5.5-2x}Zn_xPS_{4.5}CI_{1.5}|$ (x = 0, 0.1) and $In/InLi|Li_6PS_5Br|NCM-83:Li_{6-2x}Zn_xPS_5Br|$ (x = 0, 0.1) half-cells were charged to different cutoff potentials (3.5 V, 3.6 V, 3.7 V, 3.8 V and 3.9 V vs In/InLi) at 298 K, applying a C-rate of 0.1 C based on 200 mAh·g_{CAM}-1 theoretical capacity of NCM-83. Subsequently, the cells were kept at the cutoff potential for 24 h. Approximately every 30 minutes, a PEIS measurement was carried out applying an AC voltage of 10 mV in a frequency range of 7 MHz to 100 mHz, recording 15 points per decade. The cells were then further cycled at 0.1 C for 50 cycles.

Analysis of the particle size distribution. The volume-weighted particle size distribution was determined using a HELOS particle size analyzer by Sympatec. 2.5 mg of powder was placed in a small vial and dispersed in 2 ml of p-xylene with 1 wt. % polyisobutene added to enhance the viscosity and then ultrasonicated with an ultrasonic finger for approximately 15 min under inert atmosphere. Subsequently, the dispersion was injected into a cuvette containing 40 ml of p-xylene with 1 wt. % polyisobutene outside the glovebox. During the measurement the dispersion was stirred to prevent sedimentation of particles. X-ray photoelectron spectroscopy (XPS). The samples were mounted on the sample platform under inert atmosphere inside a glovebox and later transported to the XPS instrument with a sample transfer tube, also under inert atmosphere, ensuring no contact between sample and atmospheric oxygen or water. In order to conduct XPS experiments, a monochromatic Al X-ray source (1486.6 eV) running at 15 kV and 13.2 W was used on a VersaProbe II (Ulvac-Phi). It has a spectral resolution of 0.5 eV and minimal beam size of less than 100 µm. Between the sample and the analyzer, the emission angle was maintained at 45°. The data were fitted using CASA-XPS software, and additional elemental spectra were calibrated using the C 1s signal at 284.8 eV as an internal reference data point and Cu $2p_{3/2}$ (etched and surface cleaned) as external reference source. S-2p, P-2p, O-1s and Cl-2p details spectra are discussed below. Li-1s, Zn-2p, Ni-2p, Mn-2p and Co-2p detail spectra show signals but either the signal to noise ratio is not sufficient or they do not show any significant changes upon cycling and are therefore not further mentioned herein.

3. Results and discussion

3.1 Structural characterization. Two lithium argyrodite substitution series with the target compositions of $Li_{5.5-2x}Zn_xPS_{4.5}CI_{1.5}$ and $Li_{6-2x}Zn_xPS_5Br$ ($0 \le x \le 0.15$) were synthesized by a solid-state synthesis. These compositions are used to not only explore the potential incorporation of Zn^{2+} in the argyrodite structure, but also to investigate the effect of varying the halide anion. Neutron powder diffraction and powder X-ray diffraction is carried out at room temperature and the patterns are analyzed by Rietveld refinements. The co-refined neutron and X-ray powder diffraction patterns are shown in the Supporting Information Figure S2 and S3. While the neutron powder diffraction patterns have been collected to allow for distinction between the isoelectronic chloride and sulfide anions and to explore changes in the lithium-ionic substructure, X-ray diffraction was required due to the similar neutron scattering length of phosphorus and zinc, to better determine Zn^{2+} positions and occupancies.

As starting point for the co-refinements of the neutron and X-ray powder diffraction data, the structural models for $Li_{5.5}PS_{4.5}CI_{1.5}$ and for Li_6PS_5Br by Gautam *et al.*^{18,27} were used for the pristine composition of each substitution series. It is important to note, that the structural data for the Li_6PS_5Br sample heated to 550 °C and subsequently quenched in liquid nitrogen was used, as this closely resembles the synthesis procedure employed for the herein reported samples of the $Li_{6-2x}Zn_xPS_5Br$ ($0 \le x \le 0.15$) substitution series. Quenching with liquid nitrogen has been shown to significantly increase the ionic conductivity of Li_6PS_5Br and thus, was also applied herein, to obtain sufficient ionic conductivities for the application of $Li_{6-2x}Zn_xPS_5Br$ ($0 \le x \le 0.15$) as catholytes. The constraints used for the refinement and all tabulated structural data are compiled in the Supporting Information (Table S1-S10).

All investigated compositions crystallize in the cubic polymorph with space group $F\overline{4}3m$ and the lattice parameters of the pristine compositions agree well with literature data. ^{18,22} For both substitution series, the lattice parameter decreases linearly upon substitution with Zn²⁺ (Figure 2a). As the ionic radii of $r(\text{Li}^+) = 0.59 \text{ Å}$ and $r(\text{Zn}^{2+}) = 0.60 \text{ Å}^{51}$ are similar, the linear decrease of the lattice parameter is most likely a result of the higher Coulomb attraction of the divalent Zn²⁺ and the anionic framework as well as the vacancy formation. According to Vegard's law, the linearly decreasing lattice parameter indicates the formation of a solid solution in the investigated compositional space. ⁵² For Li_{5,5-2x}Zn_xPS_{4,5}Cl_{1.5}, the onset of ZnS side-phase at x = 0.15 (Table S6) along with a slightly lower refined content of Zn²⁺ compared

to the nominal Zn^{2+} content for this composition (Figure 2b) suggests the solubility limit has been reached. In the case of $Li_{6-2x}Zn_xPS_5Br$ ($0 \le x \le 0.15$), there is no structural indication that the solubility limit has already been reached for x = 0.15. However, due to lowering of the ionic conductivity upon substitution, a further investigation was deemed not feasible with the goal in mind to develop a highly conducting catholyte composition (see Section 3.2).

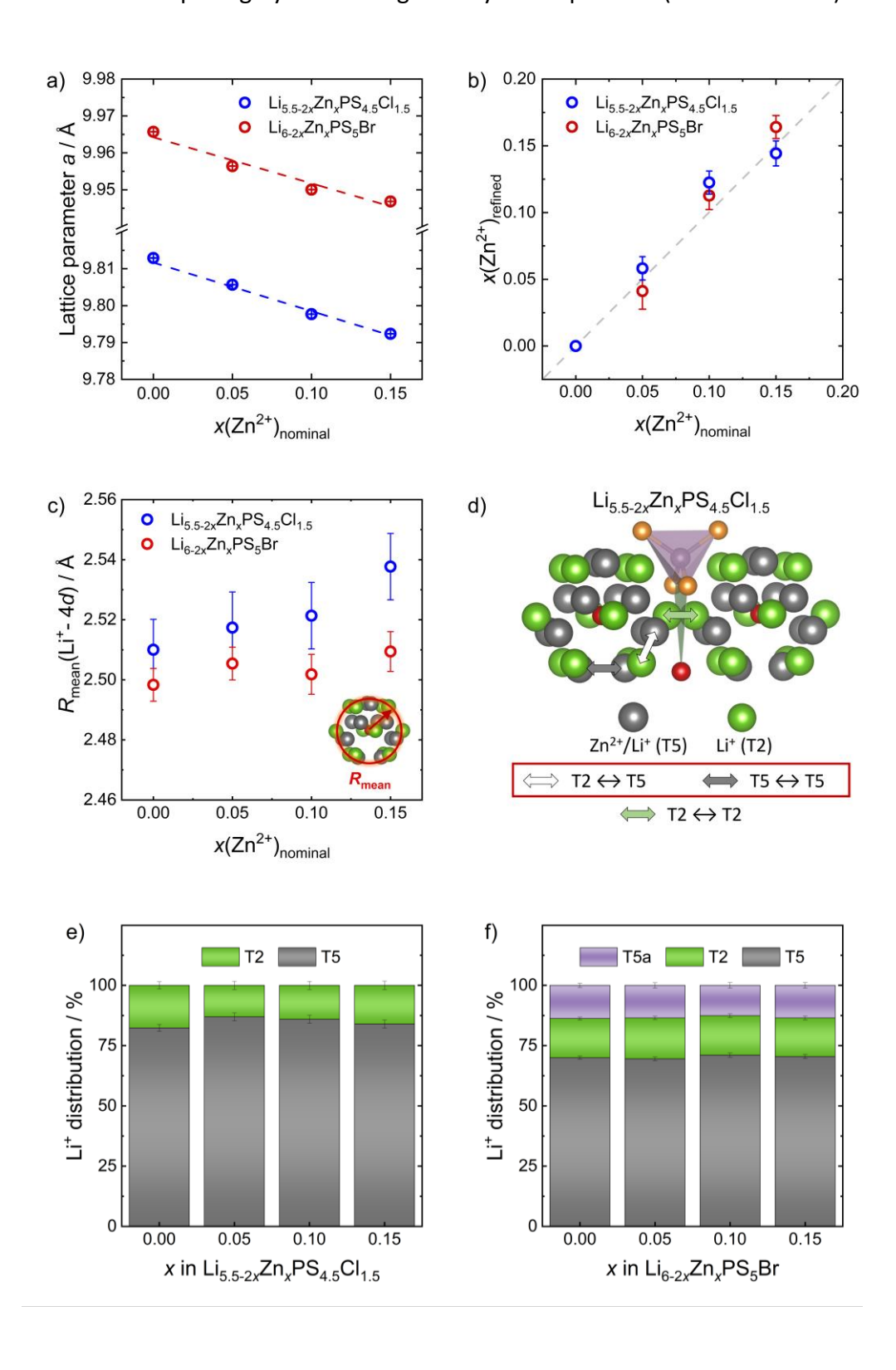


Figure 2: a) The lattice parameter decreases along with an increasing degree of Zn^{2+} substitution. b) The refined Zn^{2+} content $x(Zn^{2+})_{refined}$ agrees well with the nominal value $x(Zn^{2+})_{nominal}$. c) Increase of the mean distance of Li^+ (R_{mean}) to the center of Li^+ cages (Wyckoff 4d) along with increasing degree of substitution. d) A scheme depicting intra- and inter-cage jumps in the $Li_{5.5-2x}Zn_xPS_{4.5}Cl_{1.5}$ substitution series, which illustrates that the occupation of T5 positions by Zn^{2+} leads to blocking of intra-cage Li^+ diffusion pathways. e) and f) show that the distribution of Li^+ across the Li^+ positions remain almost unaffected by the degree of substitution in $Li_{5.5-2x}Zn_xPS_{4.5}Cl_{1.5}$ and $Li_{6-2x}Zn_xPS_5Br$. All error bars correspond to one standard deviation based on the co-refinement.

The site-occupancies of the halide and sulfide anion on Wyckoff 4a and Wyckoff 4d are in agreement with the literature reports for the pristine compositions. With increasing Zn²⁺ content a minor increase of the halide site-disorder can be observed for the Li_{6-2x}Zn_xPS₅Br $(0 \le x \le 0.15)$ substitution series from 36.0(6)% for Li₆PS₅Br to 40.2(3)% for Li_{5.7}Zn_{0.15}PS₅Br, while for Li_{5.5-2x}Zn_xPS_{4.5}Cl_{1.5} $(0 \le x \le 0.15)$, the change of the halide site-occupancies on Wyckoff 4a and 4d with increasing degree of substitution remains within the range of the refinement uncertainty (Figure S4).

For the co-refinement of the neutron and X-ray powder diffraction data, all tetrahedral voids (T1-T5)²³ were considered as possible positions for Li⁺. Additionally, all tetrahedral voids and substitutions were considered for the refinement of Zn²⁺ positions. Thereby, Li⁺ occupancy on T5 and T2 position was found for $Li_{5.5-2x}Zn_xPS_{4.5}Cl_{1.5}$ (0 $\leq x \leq$ 0.15) and Li^+ occupancy on T5, T5a and T2 position was discovered for $\text{Li}_{6-2x}\text{Zn}_x\text{PS}_5\text{Br}$ (0 $\leq x \leq$ 0.15). The found Li^+ positions and distribution for Li_{5.5}PS_{4.5}Cl_{1.5} and Li₆PS₅Br (Figure 2e and 2f) agree well with previous reports. 18,27 Interestingly, the Zn²⁺ occupancy was only found on the T5 positions for all investigated compositions, resulting in shared occupancy of the T5 position by Li⁺ and Zn²⁺. No evidence for any Zn²⁺ occupancy on other tetrahedral positions, including the phosphorus position, can be found. The refined content of Zn²⁺ agrees well with the nominal content as shown in Figure 2b. Introducing Zn²⁺ leads to a minor increase of the mean distance of cations to the cage center (R_{mean}) (Figure 2c), mainly driven by further displacement of the T5 positions away from the central anion (Figure S5). While for the $Li_{6-2x}Zn_xPS_5Br$ ($0 \le x \le 0.15$) substitution series the increased site-disorder leads to a decrease in average anionic charge in the cage center, this is not the case for the Li_{5.5-2x}Zn_xPS_{4.5}Cl_{1.5} ($0 \le x \le 0.15$) substitution series. Instead, the cage expansion may be caused by the stronger electrostatic repulsion exerted by the divalent Zn²⁺, leading to further displacement of cations from the cage center to maximize the distance between Zn²⁺ and neighboring cations. Notably, there is no evidence for the occupation of new Li⁺ sites and the overall Li⁺ distribution stays unaffected by Zn²⁺ introduction (Figure 2e and 2f). The Zn²⁺ occupation on the T5 positions is expected to disrupt Li⁺ diffusion pathways by preventing intra-cage diffusion of Li⁺ that could otherwise occur via this position. As shown in Figure 2d, Li⁺ needs to migrate via T5 positions for long-range Li⁺ transport and therefore a notable decrease of the ionic conductivity due to blocking of Li⁺ diffusion pathways should be expected.

3.2 Ionic transport. To determine the ionic conductivities and activation energies of ionic transport for the $Li_{5.5-2x}Zn_xPS_4.5Cl_{1.5}$ ($0 \le x \le 0.15$) and $Li_{6-2x}Zn_xPS_5Br$ ($0 \le x \le 0.15$) substitution series, temperature dependent electrochemical impedance spectroscopy was employed. The impedance responses, including the fits for the whole temperature range of $Li_{5.2}Zn_{0.15}PS_4.5Cl_{1.5}$ and $Li_{5.7}Zn_{0.15}PS_5Br$ and the Arrhenius plots for all compositions are given in the Supporting Information (Figure S6-S8).

While for Li_{6-2x}Zn_xPS₅Br ($0 \le x \le 0.15$) all impedance spectra can be fit with an equivalent circuit model consisting of a parallel constant phase element P and resistor R (RP element) in series with another constant phase element, this was only possible at temperatures below 273 K for Li_{5.5-2x}Zn_xPS_{4.5}Cl_{1.5} ($0 \le x \le 0.15$). At higher temperatures, the RP element shifts to frequencies that are too high to resolve due to the high ionic conductivities of these compositions. Thus, only the tails of the blocking electrodes were fit for the impedance spectra of Li_{5.5-2x}Zn_xPS_{4.5}Cl_{1.5} ($0 \le x \le 0.15$) collected at 273 K and above, using a resistor in series with a constant phase element as the equivalent circuit model. As typical for highly conducting lithium argyrodites, bulk and grain boundary contributions cannot be deconvoluted. The ideality of the processes ($\alpha > 0.9$) as well as the capacitances between $1 \cdot 10^{-11}$ F and $2 \cdot 10^{-10}$ F suggest the ionic transport is dominated by the bulk. 14,53

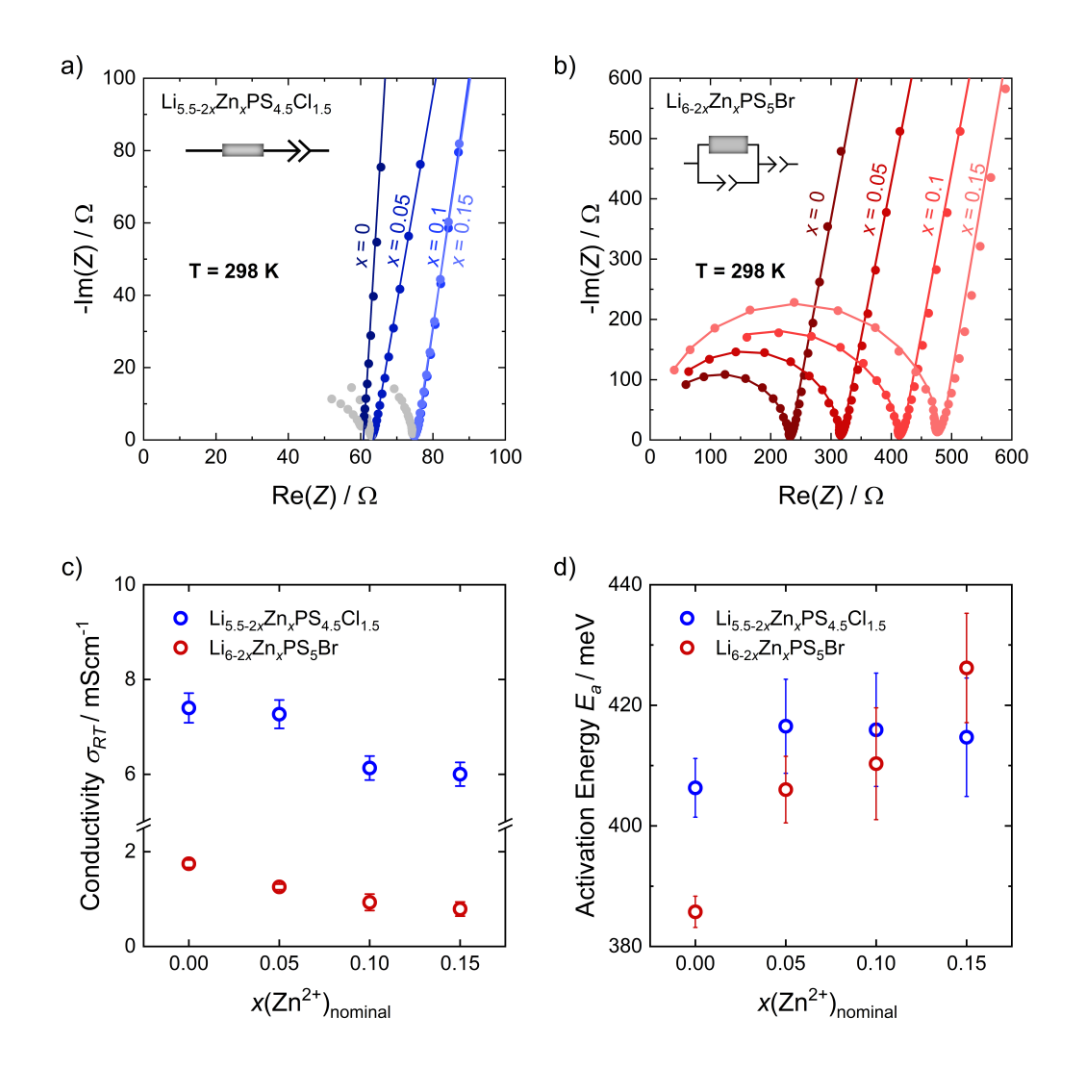


Figure 3: Impedance spectra of a) $Li_{5.5-2x}Zn_xPS_{4.5}Cl_{1.5}$ and of b) $Li_{6-2x}Zn_xPS_5Br$ at room temperature including the fit and the corresponding equivalent circuit model, showing the increase of resistance due to Zn^{2+} substitution. c) Ionic conductivities σ_{RT} at room temperature decreases with $x(Zn^{2+})_{nominal}$. d) Activation energies E_a increase along with $x(Zn^{2+})_{nominal}$. The error bars resemble errors from fitting of the data. Datapoints that were not fit due to the Kramers-Kronig relation are shown in grey.

All impedance spectra measured at 298 K, including the respective fits are given in Figure 3a and 3b. The room temperature conductivity of the pristine compositions of 7.4(3) mS·cm⁻¹ for Li_{5.5}PS_{4.5}Cl_{1.5} and 1.7(1) mS·cm⁻¹ for Li₆PS₅Br are in agreement with previous reports. ^{18,27} Furthermore, the relative pellet densities within each substitution series remain comparable, indicating the conductivity trends do not originate from variation in the porosity and must indeed be a result of the structural changes induced by Zn²⁺ introduction. ⁵⁴ As shown in Figure 3c the room temperature ionic conductivity of Li_{5.5-2x}Zn_xPS_{4.5}Cl_{1.5} decreases along with an increasing fraction of Zn²⁺ down to 6.0(3) mS·cm⁻¹ for x = 0.15. Similarly, a decrease in room

temperature ionic conductivity down to $0.8(1) \text{ mS} \cdot \text{cm}^{-1}$ for x = 0.15 was observed for $\text{Li}_{6-2x}\text{Zn}_x\text{PS}_5\text{Br}$. The decline in room temperature ionic conductivities along with an increasing degree of substitution is accompanied by an increase of the activation energies from 406(5) meV to 415(10) meV for $\text{Li}_{5.5-2x}\text{Zn}_x\text{PS}_{4.5}\text{Cl}_{1.5}$ and from 386(3) meV to 426(9) meV for $\text{Li}_{6-2x}\text{Zn}_x\text{PS}_5\text{Br}$, which indicates a significant impact of Zn^{2+} substitution on the potential energy landscape.

Besides the increasing occupation of the Li⁺ T5 position by Zn²⁺, which blocks Li⁺ transport pathways (Figure 2b and 2d), the decrease in charge carrier density and the slight decrease in unit cell volume (and thus bottleneck sizes) may further contribute to the decrease of ionic conductivity upon Zn²⁺ introduction. The detrimental effects of these structural changes may be attenuated by an increase in R_{mean} (Figure 2c), which is usually associated with an increase of ionic conductivities.¹⁸ Nevertheless, since the changes of the charge carrier density, unit cell volume and R_{mean} are rather small, only minor influences are expected. Due to the successful introduction of Zn²⁺ and their high ionic conductivities these materials are ideal candidates to test how Zn²⁺ substitution of lithium argyrodite catholytes affects cathode performance and (electro-)chemical decomposition.

3.3 Solid-state battery cycling. To evaluate the effects of Zn^{2+} substitutions in $Li_{5.5-2x}Zn_xPS_{4.5}Cl_{1.5}$ and $Li_{6-2x}Zn_xPS_5Br$ on the performance of solid-state batteries, cycling experiments on half-cells incorporating $Li_{5.5-2x}Zn_xPS_{4.5}Cl_{1.5}$ (x = 0, 0.1) and $Li_{6-2x}Zn_xPS_5Br$ (x = 0, 0.1) catholytes were performed. As the goal is to study the effect of Zn^{2+} substitution on CEI formation and to explore the concept of CEI design by substitution of lithium argyrodites, only the composition of the catholyte is varied, while the pristine composition of each substitution series was used as separator. For both substitution series, the composition with nominal substitution x = 0.1 was chosen as catholyte to compare the performance against the pristine composition. While for the $Li_{5.5-2x}Zn_xPS_{4.5}Cl_{1.5}$ this was due to the onset of ZnS sidephase at x = 0.15, for $Li_{6-2x}Zn_xPS_5Br$ the ionic conductivity for x = 0.15 below 1 mS·cm⁻¹ was deemed to be too low to apply this material as catholyte in solid-state batteries.

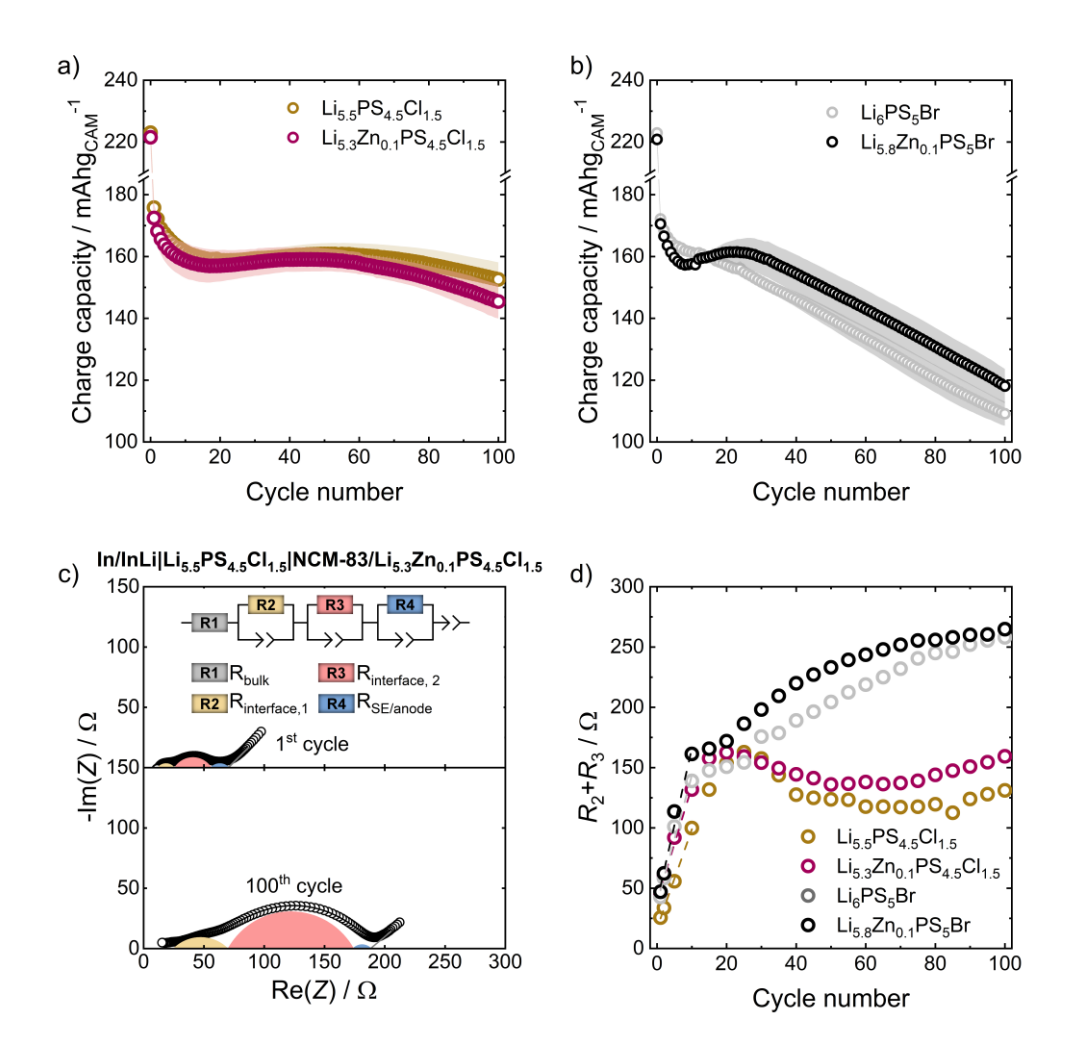


Figure 4: Charge capacities of a) $In/InLi|Li_{5.5}PS_{4.5}CI_{1.5}|NCM-83:Li_{5.5-2x}Zn_xPS_{4.5}CI_{1.5}$ (x = 0, 0.1) half-cells and b) $In/InLi|Li_6PS_5Br|NCM-83:Li_{6-2x}Zn_xPS_5Br$ (x = 0, 0.1) half-cells as a function of the cycle number. The error bars correspond to the standard deviation from triplicate cell cycling. c) Nyquist plots of the impedance data of an $In/InLi|Li_{5.5}PS_{4.5}CI_{1.5}|NCM-83:Li_{5.3}Zn_{0.1}PS_{4.5}CI_{1.5}$ cell after the 1^{st} and 100^{th} charge cycle, including the corresponding fit and equivalent circuit model. d) Evolution of R_2+R_3 after charging as measure of the CEI resistance as a function of the cycle number. The dashed lines are added as guide for the eye to indicate the increase of R_2+R_3 in the first ten charge cycles.

In Figure 4a, the charge capacities of half-cells with $Li_{5.5-2x}Zn_xPS_{4.5}Cl_{1.5}$ (x = 0, 0.1) as catholyte and cycled at 0.1 C are shown. The respective charge discharge curves are given in Figure S9. Each half-cell setup was tested in triplicates to ensure reproducibility and avoid mis- or overinterpretation of trends. In the first cycle, all cells have a high charge capacity over 220 mAh·g_{CAM}⁻¹ as typical for NCM with high nickel content,^{4,55} followed by an irreversible capacity loss after the first cycle of over 40 mAh·g_{CAM}⁻¹. The fast capacity loss, which is

especially observed in the first cycle, but also up to the 10th cycle is typically thought to originate from a combination of oxidative decomposition of the catholyte at elevated potentials leading to the formation of a resistive CEI layer and contact loss due to volume expansion/contraction during (de-)lithiation of NCM-83 particles. 56,57 Interestingly, from the 20th to the 50th cycle the capacity fading stops entirely, and the capacity even increases slightly. This phenomenon is potentially caused by the redox activity of the decomposition products formed during the decomposition of the solid electrolyte.^{30,58} From the 50th cycle onwards, increasing capacity fading is observed, indicating propagating (electro-)chemical decomposition reactions. This is reflected in the charge discharge curves and increasing voltage hysteresis, as result of the higher overpotentials during charging and discharging (Figure S9 and S10).⁵⁶ The cycling performance of cells using Li_{5.3}Zn_{0.1}PS_{4.5}Cl_{1.5} catholyte appears to be slightly worse, showing faster capacity fading in the initial cycles and also at higher cycle numbers. In Figure 4b, the charge capacities of half-cells with $Li_{6-2x}Zn_xPS_5Br$ (x = 0, 0.1) catholytes cycled at a charging rate of 0.1 C are shown. Despite quite similar initial capacities compared to the cells with $Li_{5.5-2x}Zn_xPS_{4.5}Cl_{1.5}$ (x = 0, 0.1) catholytes, continuous capacity fading starts already before the 30th cycle and is more severe.

To better gauge the underlying reasons for the observed trends of charge capacities, impedance data after each charge cycle were collected. In Figure 4c, the impedance data of a half-cell with Li_{5.3}Zn_{0.1}PS_{4.5}Cl_{1.5} catholyte are shown after the 1st and 100th charge cycle, including the corresponding fits. Additionally, the equivalent circuit used for fitting all impedance data of half-cells in this study, assuming four different processes, is shown. These processes typically represent the bulk resistance of the solid electrolyte R_{SE,bulk} (gray), a resistance with the capacitance of grain boundaries R_{SE,grain} (yellow), the resistance at the interface between solid electrolyte and cathode active material R_{SE/CAM} (red) and the resistance at the interface of the solid electrolyte and the anode material $R_{SE/anode}$ (blue). The processes were assigned based on the capacitances of the RP-elements and the frequency range, analogous to previous reports. 30,55,59,60 In this study, the four corresponding resistances are labelled R_1 , R_2 , R_3 and R_4 , as these cannot all unequivocally be assigned to a known physical process. While the first resistance R_1 in the high-frequency range can clearly be assigned to the bulk transport of the solid electrolyte and R₄ could be assigned to the resistance at the interface of the solid electrolyte and the anode material $R_{SE/anode}$, the distinction between R_2 and R_3 is especially challenging. The corresponding processes have a strong overlap of time constants, as indicated by low α -values, which leads to large errors of the fitting parameters. Thus, $R_2 + R_3$ represents the best obtainable approximation of the growing resistance resulting from CEI formation at the SE/CAM interface during cycling.⁵³ The impedance data after the 1st and 100th charge cycle including all remaining cell setups for cycling experiments are shown in Figure S10 in the Supporting Information.

The evolution of $R_2 + R_3$ as a function of cycle number (Figure 4d) shows a strong increase in the first 10 cycles when using $\text{Li}_{6-2x}\text{Zn}_x\text{PS}_5\text{Br}$ (x=0,0.1) catholytes and in the first 20 cycles for $\text{Li}_{5.5-2x}\text{Zn}_x\text{PS}_{4.5}\text{Cl}_{1.5}$ (x=0,0.1) catholytes. This increase of $R_2 + R_3$ indicates that most of the CEI formation occurs within the first cycles, which is in line with previous reports. ^{29,56} Furthermore, the faster increase of $R_2 + R_3$ for cells with $\text{Li}_{6-2x}\text{Zn}_x\text{PS}_5\text{Br}$ (x=0,0.1) catholytes suggests faster CEI growth kinetics and/or the formation of more resistive decomposition products. These results are in agreement with the cycling data and voltage hysteresis (Figure S11), where all cells exhibit rapid capacity fading in the initial charge cycles along with increasing overpotentials during charge and discharge.

Interestingly, when comparing the slope of $R_2 + R_3$ for cells with and without Zn^{2+} for either substitution series as marked by dashed lines in Figure 4d, the cells with Zn²⁺ generally show a faster initial increase of $R_2 + R_3$. This indicates, that there are differences in the growth kinetics and/or decomposition products formed at the SE/CAM interface. After this initial increase, the evolution of $R_2 + R_3$ starts to strongly deviate when comparing cells incorporating $\text{Li}_{5.5-2x}\text{Zn}_x\text{PS}_{4.5}\text{Cl}_{1.5}$ (x = 0, 0.1) and $\text{Li}_{6-2x}\text{Zn}_x\text{PS}_5\text{Br}$ (x = 0, 0.1) catholytes. While $R_2 + R_3$ stabilizes for cells with $Li_{5.5-2x}Zn_xPS_{4.5}Cl_{1.5}$ (x = 0, 0.1) catholytes, cells containing $Li_{6-2x}Zn_xPS_5Br$ (x = 0, 0.1) catholytes show a continuous increase of $R_2 + R_3$, causing the fast capacity fading of in contrast to the stable cycling performance for half-cells using Li_{5.5-2x}Zn_xPS_{4.5}Cl_{1.5} (x = 0, 0.1) catholytes. This deviation in cycling performance and $R_2 + R_3$ demonstrate superior performance of the Li_{5.5-2x}Zn_xPS_{4.5}Cl_{1.5} catholytes compared to the Li_{6-2x}Zn_xPS₅Br catholytes, which cannot be explained by their higher ionic conductivity alone. While the halide does not participate in oxidative degradation⁶¹, the phosphorus and sulfur containing decomposition products formed at the SE/CAM interphase likely differ and are more suitable at preventing further degradation in case of the Li_{5.5-2x}Zn_xPS_{4.5}Cl_{1.5} catholytes. When comparing Zn²⁺ substituted and unsubstituted catholytes of one substitution series, it appears that the Zn²⁺ substituted catholytes show a slightly higher $R_2 + R_3$ until the 100th cycle. At this point it remains unclear, whether this is a result of different CEI growth kinetics or differences in chemical composition of the CEI and is therefore further explored in the following sections.

3.4 Kinetics of CEI formation. Motivated by the finding that $R_2 + R_3$ increases faster when using Zn^{2+} substituted lithium argyrodites, the kinetics of the degradation reactions at the SE/CAM interface that lead to the formation of the CEI were further investigated. Thermodynamically the oxidative decomposition is mostly governed by the sulfur band edges. Therefore, the influence of thermodynamics can be considered to only play a minor role when comparing the CEI formation of the Zn^{2+} substituted and unsubstituted materials. Due to the significantly worse cycling performance of $Li_{6-2x}Zn_xPS_5Br$ (x=0,0.1), it is obvious that these materials are unsuitable for building high-performance solid-state batteries. Hence, these catholytes were excluded from further studies to entirely focus on the degradation kinetics of $Li_{5.5-2x}Zn_xPS_{4.5}Cl_{1.5}$ (x=0,0.1) hereinafter. To rule out that the particle size distributions of the catholyte and the cathode porosity have an influence on the observed differences in cycling performance, both were determined experimentally for each catholyte. Due to the similar synthesis procedure and processing conditions, similar particle size distributions and cathode porosity are expected and were also confirmed experimentally (Figure S12).

Previous work by Zuo *et al.* on oxidative degradation at the LGPS|NCM-622 interface has shown that the cutoff potential strongly influences the kinetics of degradation as well as the degradation products formed at SE|CAM interfaces.³⁴ To explore the degradation kinetics in the Zn²⁺ substituted catholytes, here the cutoff potentials 3.5 V, 3.6 V, 3.7 V, 3.8 V and 3.9 V versus In/InLi are considered. To study the CEI formation, all half-cells (x = 0, 0.1) were first charged to the respective cutoff potential and then held at that potential for 24 h. During that time, impedance spectra were measured every 30 minutes as illustrated in Figure 5a. After the 24 h potential hold, the cells were discharged and then cycled for another 50 cycles at the respective cutoff potential. The impedance data collected during the period of potential hold were analyzed using the same equivalent circuit model as applied for the evaluation of the cycling of half-cells using Li_{5.5-2x}Zn_xPS_{4.5}Cl_{1.5} (x = 0, 0.1) catholytes (Figure 4c).

Based on previous works, a Wagner-type model for diffusion-controlled reactions was employed to describe the growth of the CEI.^{34,62} Since the CEI formation is diffusion-controlled a coupled migration of ionic and electronic charge carriers is required. The lithium chemical potential difference across the CEI acts as the driving force for the CEI growth and is controlled

by the state of charge (degree of lithiation of NCM), all of which corresponds to the potential that is held constant. Assuming that charge transport of ions is significantly faster than the electron transport across the CEI, equation (1) can be used to describe the time dependence of the growth of CEI resistance (R_{CEI}).

$$R_{\text{CEI}} = \frac{1}{S\overline{\sigma}_{\text{CEI}}} \sqrt{\frac{V_{\text{m}}}{xF^{2}} \cdot \frac{\overline{\sigma}_{\text{Li}^{+}} \cdot \overline{\sigma}_{\text{e}^{-}}}{\overline{\sigma}_{\text{Li}^{+}} + \overline{\sigma}_{\text{e}^{-}}}} \cdot \Delta \mu_{\text{Li}} \cdot \sqrt{t} = \frac{1}{S\overline{\sigma}_{\text{CEI}}} \cdot k \cdot \sqrt{t} = k^{*} \cdot \sqrt{t}$$
 (1)

In equation (1), S represents the surface area passed by Li⁺ and electrons, $\bar{\sigma}_{CEI}$ denotes the average conductivity of the CEI, $V_{\rm m}$ represents the average molar CEI volume, x denotes the moles of Li extracted from Li_{5.5-2x}Zn_xPS_{4.5}Cl_{1.5} (x = 0, 0.1), F represents Faraday's constant, $\bar{\sigma}_{\rm Li^+}$ and $\bar{\sigma}_{\rm e^-}$ denote the mean partial lithium-ion and electronic conductivity of the CEI and $\Delta\mu_{\rm Li}$ represents the chemical potential gradient of lithium across the CEI. The equation can be simplified by introducing a rate constant for the growth rate in terms of thickness k and can be even further simplified by introducing k^* reflecting the growth rate in terms of resistance.

The result of the diffusion-controlled growth rate is a linear growth behavior of $R_2 + R_3$ (representing R_{CEI} here) versus $t^{0.5}$, which can be observed for all half-cells up to a cutoff potential of 3.7 V vs In/InLi (Figure 5b, Figure S13a and S13b). Interestingly, in contrast to LGPS|NCM-622 composites held at 3.8 V and 3.9 V vs In/InLi, the herein investigated half-cells only initially follow parabolic growth behavior (Figure S13c and S13d), until they transition to linear growth behavior (Figure S14). This indicates that the Wagner-type model for diffusion-controlled reactions is not sufficient to describe the growth behavior of the CEI at 3.8 V and 3.9 V vs In/InLi after a critical thickness of the CEI is reached. The transition from parabolic to linear growth behavior may be caused by superposition of the chemical diffusion by electric field driven ionic currents, as it has been observed for solid-state reactions of spinels. Nevertheless, to enable a comparison at least for the initial CEI growth, only the portion of the data following parabolic growth behavior was included for the fit and extraction of k^* at 3.8 V and 3.9 V versus In/InLi.

The average growth rate of the CEI resistance k^*_{mean} was calculated from the linear fits of the triplicates of $R_2 + R_3$ versus $t^{0.5}$ for each cutoff potential and catholyte composition and is given in Figure 5c. For 3.5 V to 3.7 V versus In/InLi a linear dependence of $k^* \sim \Delta \mu_{\text{Li}}$ and thus roughly to the potential can be observed. For 3.8 V and 3.9 V versus In/InLi, k^*_{mean} grows much faster

as it would be expected from $k^* \sim \Delta \mu_{\text{Li}}$, suggesting there are factors beyond the state of charge such as changes in the partial ionic and electronic conductivity to consider, which will be further discussed in Section 3.5. Compared to LGPS|NCM-622 composites, the growth rate k^* is generally larger for each potential, indicating the formation of more detrimental decomposition products at the Li_{5.5-2x}Zn_xPS_{4.5}Cl_{1.5} (x = 0, 0.1)|NCM-83 interface.

At potentials from 3.5 V to 3.7 V vs In/InLi, the growth rate k^*_{mean} of cells incorporating Li_{5.3}Zn_{0.1}PS_{4.5}Cl_{1.5} as catholyte is slightly higher as compared to Li_{5.5}PS_{4.5}Cl_{1.5}, which points towards faster degradation or the formation of more unsuitable degradation products as for Li_{5.5}PS_{4.5}Cl_{1.5} (Figure S13a and S13b). Here, decomposition products based on ZnS or related semiconducting species may be possible. This would lead to a higher partial electronic conductivity of the CEI. Since the growth rate is limited by the charge carrier with the smaller partial conductivity according to equation (1), which in this case is the partial electronic conductivity, this may explain the faster decomposition kinetics of the Zn²⁺ substituted materials. At 3.8 V and especially 3.9 V versus In/InLi (Figure S13c and S13d), the differences of $R_2 + R_3$ are within the standard deviation of the triplicate data and therefore do not allow for identification of significant differences of the CEI growth kinetics when using the substituted and pristine catholyte at these cutoff potentials.

3.5 Cycling at different cutoff potentials. In order to investigate the influence of the decomposition products on cycling of half-cells with $Li_{5.5-2x}Zn_xPS_{4.5}Cl_{1.5}$ (x = 0, 0.1) composites and thus gain further insights into the effect of Zn^{2+} substitution on CEI formation and cell performance, duplicates of half-cells that were previously held at 3.5 V, 3.6 V, 3.7 V, 3.8 V, and 3.9 V versus In/InLi for 24 hours were cycled for 50 cycles to the respective cutoff potential at 0.1 C. It has been shown for LGPS | NCM-622 composites that the CEI compositions may differ depending on the cutoff potential, which may fundamentally influence the cycling behavior.³⁴ Additionally, the formation of a thicker CEI layer occurs at higher cutoff potentials, potentially making differences between the CEI formation of Zn^{2+} substituted and unsubstituted materials more apparent.

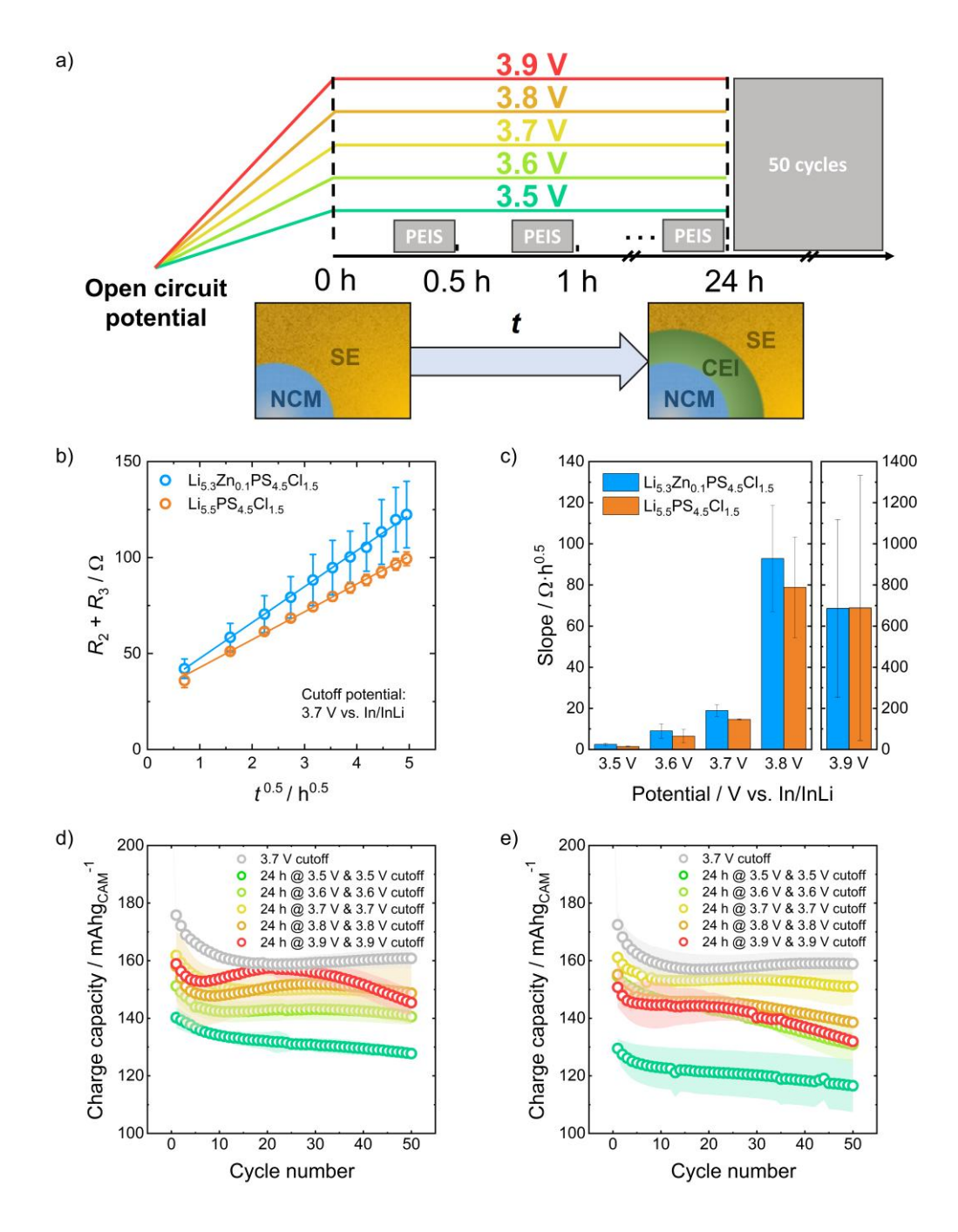


Figure 5: a) Illustration of the protocol used for the potential dependent investigation of the kinetics for CEI formation. b) Linear fits of the average R_2+R_3 obtained from the impedance data as a function of $t^{0.5}$ of cells tested at 3.7 V vs In/InLi. Error bars correspond to the standard deviation from triplicate measurements. c) Comparison of the average slopes extracted from the R_2+R_3 vs $t^{0.5}$ plots as a measure of the mean growth rate k^*_{mean} for each cell setup and potential. Charge capacities of d) In/InLi|Li_{5.5}PS_{4.5}Cl_{1.5}|NCM-83:Li_{5.5}PS_{4.5}Cl_{1.5}| half-cells and e) In/InLi|Li_{5.5}PS_{4.5}Cl_{1.5}|NCM-83:Li_{5.3}Zn_{0.1}PS_{4.5}Cl_{1.5} half-cells as a function of the cycle number. All half-cells except for the comparison in grey have previous been held at a certain potential for

24 h and are then cycled using the same potential as cutoff potential. The error bars correspond to the standard deviation from duplicate measurements.

In Figure 5d and 5e the charge capacities of the half-cells with Li_{5.5-2x}Zn_xPS_{4.5}Cl_{1.5} (x = 0, 0.1) catholytes are shown. For each catholyte, the half-cells which were cycled to a cutoff potential of 3.7 V versus In/InLi, show the highest overall charge capacities and high capacity retention (Figure S15). At this cutoff potential, most of the capacity of NCM-83 can be accessed as indicated by the charge discharge curves (Figure S16), while the growth rate of the CEI and thus the resulting cell resistance is still relatively low as compared to the cells cycled up to 3.8 V or 3.9 V versus In/InLi (Figure 5c), leading to good capacity retention. These findings are corroborated by the evolution of the CEI resistance $R_2 + R_3$ extracted from PEIS measurements after the 24 h decomposition step and after the following charge cycles of the half-cells (Figure S17).

The most pronounced differences between the cycling performance of Zn²⁺ substituted and unsubstituted catholytes can be seen for the cells cycled at 3.8 V and 3.9 V versus In/InLi. Whereas higher charge capacities can be achieved for cells with the Li_{5.5}PS_{4.5}Cl_{1.5} catholyte, the obtainable charge capacities are lower when employing Li_{5.3}Zn_{0.1}PS_{4.5}Cl_{1.5} as the catholyte, suggesting that the CEI is more detrimental for Li_{5.3}Zn_{0.1}PS_{4.5}Cl_{1.5}, especially at higher cutoff potentials.

To attain chemical information on the degradation products formed at the catholyte | NCM-83 interface, X-ray photoelectron spectroscopy was performed. In Figure 6a and 6b the S-2p and P-2p detail spectra are shown, and the O-1s and Cl-2p detail spectra can be seen in Figure S18 and S19. Zn-2p spectra were also recorded, but no signal was visible due to the small amount of zinc present in the cathode composite. Spectra are shown for the uncycled cathode composites as well as for $\text{Li}_{5.5-2x}\text{Zn}_x\text{PS}_{4.5}\text{Cl}_{1.5}$ (x=0,0.1) | NCM-83 cathode composites after 50 cycles with a cutoff potential of 3.7 V vs In/InLi and 3.8 V vs In/InLi from the cycling experiments above.

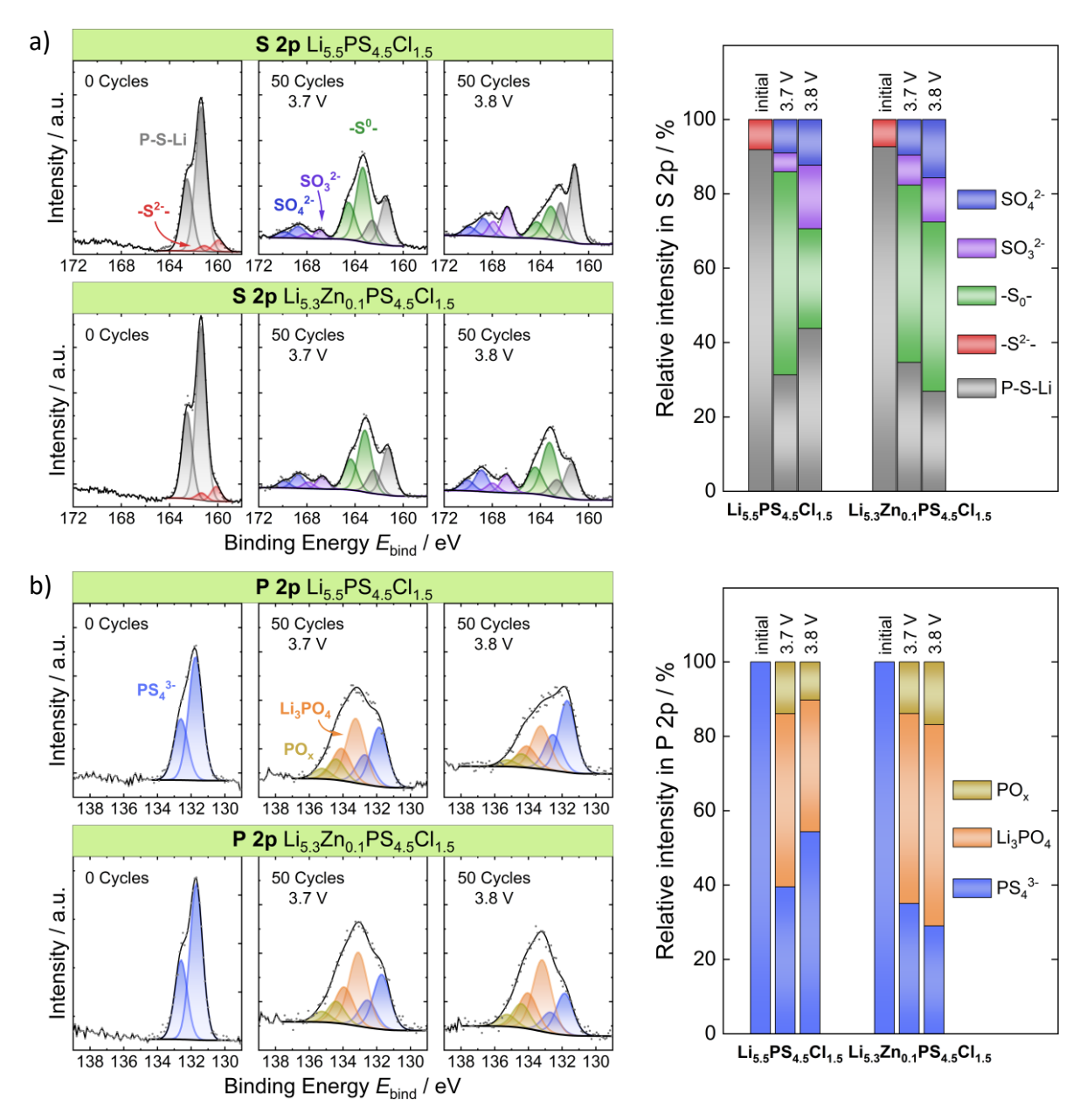


Figure 6: XPS spectra and relative intensities of species identified from the fit of a) S-2p and b) P-2p signals of cathode composites including $Li_{5.5}PS_{4.5}Cl_{1.5}$ and $Li_{5.3}Zn_{0.1}PS_{4.5}Cl_{1.5}$ as catholyte before cycling and after cycling to a cutoff potential of 3.7 V or 3.8 V.

In the S-2p detail spectra shown in Figure 6a, the signals before cycling could be assigned to the $(PS_4)^{3-}$ tetrahedra (161.4 eV) and free S^{2-} (159.9 eV) of the argyrodite structure. After cycling, oxidative degradation products are formed, which include polysulfides, as indicated by the presence of -S₀- groups at higher binding energies (163.4 eV)^{29,65}, sulfites (166.9 eV)⁶⁴ and sulfates (168.7 eV). Furthermore, the degradation leads to weakening of the $(PS_4)^{3-}$ signals and disappearance of the free S^{2-} signals of the argyrodite structure. The P-2p spectra in Figure 6b corroborate the presence of $(PS_4)^{3-}$ units (132.7 eV)⁶⁴ and further indicate the

formation of Li₃PO₄ (133.2 eV) and PO_x species (134.4 eV)^{29,65,67} as additional oxidative degradation products during cell cycling. The presence of Li₃PO₄ (531.3 eV)⁶⁵ and Li₂SO₄⁶⁸ after cycling was verified by the O-1s detail spectra (Figure S18). These show the presence of both compounds even before cycling of the cells, which likely results from surface impurities of the argyrodite and NCM-83 and has been previously observed by *Walther et al.*²⁹ The Cl-2p signal spectra do not show any changes upon cycling (Figure S19), confirming Cl⁻ is not involved in the oxidative degradation.⁶¹ While Zn-2p detail spectra were also recorded, the signal to noise ratio was not sufficient to allow for assignment of Zn species. Nevertheless, decomposition products based on ZnS or related semiconducting species may be conceivable that result in an increased electronic conductivity of the CEI, leading to faster decomposition kinetics. This is reflected by the higher relative intensity of decomposition products in the XPS spectra when employing Li_{5.3}Zn_{0.1}PS_{4.5}Cl_{1.5} as shown in Figure 6. Redox activity of Zn²⁺ such as reduction to Zn is not expected in the potential window in which the cycling experiments were performed.

Interestingly, the relative intensities of the oxidative degradation products in the S-2p, P-2p and O-1s detail spectra after cycling to a cutoff potential of 3.7 V vs In/InLi for 50 cycles at 0.1 C reported herein are significantly higher in comparison to the XPS spectra reported by Walther *et al.* for Li₆PS₅CI|NCM-622 cathode composites after 100 cycles with the same cutoff potential and C-rate.²⁹ Additionally, sulfites and sulfates were not found at the Li₆PS₅CI|NCM-622 interface. The significant differences in the decomposition behavior potentially stems from the 24 h hold at the cutoff potential before cycling as well as the higher structural instability of NCM-83 and Li_{5.5}PS_{4.5}Cl_{1.5}.⁴¹

For both catholytes, the cells with 3.8 V vs In/InLi cutoff potential generally show more oxidative degradation products, which is in line with the results obtained from the cycling experiments. While the amount of phosphorous-based degradation products (PO_x and Li_3PO_4) remains mostly unchanged, more sulfuric degradation products are formed. Notably, there is a shift towards sulfite- and sulfate-based degradation products with increasing cutoff potential, whereas the signals corresponding to polysulfides remain similar or even decrease in intensity in the case of the $Li_{5.5}PS_{4.5}Cl_{1.5}$ catholyte. The shift towards oxygenated degradation products agrees with previous works, that suggests a significant increase of oxygen release once NCM-811 is charged to a potential above 4.3 V vs Li^+/Li (≈ 3.7 V vs In/InLi). 34,41,69,70

The relative amount of decomposition products including SO_x, PO_x and polysulfides that are observed by XPS when comparing Li_{5.3}Zn_{0.1}PS_{4.5}Cl_{1.5} and Li_{5.5}PS_{4.5}Cl_{1.5} catholytes are similar at 3.7 V vs In/InLi, which is in agreement with the similar cycling behavior at that cutoff potential. At 3.8 V vs In/InLi more pronounced decomposition occurs for the Li_{5.3}Zn_{0.1}PS_{4.5}Cl_{1.5} catholyte as indicated by lower intensity of signals corresponding to (PS₄)³⁻ units in the S-2p and P-2p detail spectra. This aligns with the worse cycling behavior observed for the cells with Li_{5.3}Zn_{0.1}PS_{4.5}Cl_{1.5} catholyte at 3.8 V vs. In/InLi and highlights again that Li_{5.3}Zn_{0.1}PS_{4.5}Cl_{1.5} has faster decomposition kinetics, which becomes more apparent at high cutoff potentials as a result of the increased thickness of the CEI.

Conclusions

The structure-transport correlation of Li_{5.5-2x}Zn_xPS_{4.5}Cl_{1.5} ($0 \le x \le 0.15$) and Li_{6-2x}Zn_xPS₅Br ($0 \le x \le 0.15$) \leq 0.15) and interfacial degradation of Li_{5.5-2x}Zn_xPS_{4.5}Cl_{1.5} (x = 0, 0.1)|NCM-83 and Li_{6-2x}Zn_xPS₅Br (x = 0, 0.1) | NCM-83 composites were investigated to explore the concept of CEI design by elemental substitution. By using a combination of high-resolution neutron diffraction and Xray diffraction, the blocking of Li⁺ transport pathways through occupation of T5 positions within the Li⁺ cages by Zn²⁺ was found and was related to the decrease of the roomtemperature ionic conductivity along with increasing activation energies. Cycling experiments of solid-state batteries incorporating the pristine and Zn²⁺ substituted materials as catholytes, unveil quicker capacity fading when using Zn²⁺ substituted argyrodites as catholytes, along with higher CEI resistances after charging. The decomposition kinetics of Li_{5.5-2x}Zn_xPS_{4.5}Cl_{1.5} (x = 0, 0.1) NCM-83 composites were quantitively evaluated by state-of-charge dependent studies, revealing slightly faster degradation kinetics in the case of Li_{5.3}Zn_{0.1}PS_{4.5}Cl_{1.5} and a strong increase of the CEI growth rate for cutoff potentials above 3.7 V vs In/InLi, which was further reflected in faster capacity fading observed in subsequent cycling experiments. Analyses of X-ray photoemission detail spectra unveil a shift towards more oxygenated decomposition products at a cutoff potential ≥ 3.8 V vs. In/InLi, including sulfites and sulfates, and confirm that Li_{5.3}Zn_{0.1}PS_{4.5}Cl_{1.5} is more prone to oxidative decomposition compared to unsubstituted Li_{5.5}PS_{4.5}Cl_{1.5}.

Overall, this work shows that the composition of the catholyte affects kinetics of CEI formation and the chemical composition of the CEI. While Zn²⁺ substitution does not lead to the desired

improved growth kinetics and composition of the CEI, other elemental substitutions may enable the design of a CEI with more favorable properties.

Supporting Information

- Rietveld refinements of neutron and x-ray diffraction patterns, refinement constraints and structural data, Wyckoff 4a and 4d halide site-occupancy, distance of T5 position to the center of Li⁺ cages, temperature-dependent impedance spectra, Arrhenius plots, charge and discharge curves, voltage hysteresis, impedance spectra of half-cells after charging including the fit, linear fits of the R_2+R_3 as a function of $t^{0.5}$ and t, evolution of R_2+R_3 as function of cycle number for cells cycled to different cutoff potentials, O-1s and Cl-2p X-ray photoelectron spectroscopy detail spectra
- Crystallographic information files

Acknowledgments

The authors acknowledge financial support within the cluster of competence FESTBATT funded by the Bundesministerium für Bildung und Forschung (BMBF; project 03XP0430F). We further acknowledge funding from the Deutsche Forschungsgemeinschaft under project number 459785385. O.M. is member of the International Graduate School for Battery Chemistry, Characterization, Analysis, Recycling and Application (BACCARA), which is funded by the Ministry for Culture and Science of North Rhine-Westphalia, Germany. This research used resources at the Spallation Neutron Source (IPTS-30876.1), a DOE Office of Science User Facility operated by the Oak Ridge National Laboratory.

Conflict of Interest

The authors declare no conflict of interest.

Data Availability Statement

The data that support the findings of this study have been archived at https://doi.org/10.17879/85978559595.

References

- (1) Janek, J.; Zeier, W. G. Challenges in Speeding up Solid-State Battery Development. *Nat. Energy* **2023**, *8* (3), 230-240. https://doi.org/10.1038/s41560-023-01208-9.
- (2) Krauskopf, T.; Richter, F. H.; Zeier, W. G.; Janek, J. Physicochemical Concepts of the Lithium Metal Anode in Solid-State Batteries. *Chem. Rev.* **2020**, *120* (15), 7745–7794. https://doi.org/10.1021/acs.chemrev.0c00431.
- (3) Tan, D. H. S.; Chen, Y. T.; Yang, H.; Bao, W.; Sreenarayanan, B.; Doux, J. M.; Li, W.; Lu, B.; Ham, S. Y.; Sayahpour, B.; Scharf, J.; Wu, E. A.; Deysher, G.; Han, H. E.; Hah, H. J.; Jeong, H.; Lee, J. B.; Chen, Z.; Meng, Y. S. Carbon-Free High-Loading Silicon Anodes Enabled by Sulfide Solid Electrolytes. *Science* 2021, 373 (6562), 1494–1499. https://doi.org/10.1126/science.abg7217.
- (4) Schlautmann, E.; Weiß, A.; Maus, O.; Ketter, L.; Rana, M.; Puls, S.; Nickel, V.; Gabbey, C.; Hartnig, C.; Bielefeld, A.; Zeier, W. G. Impact of the Solid Electrolyte Particle Size Distribution in Sulfide-Based Solid-State Battery Composites. *Adv. Energy Mater.* **2023**, No. *2302309*, 1–9. https://doi.org/10.1002/aenm.202302309.
- (5) Minnmann, P.; Quillman, L.; Burkhardt, S.; Richter, F. H.; Janek, J. Editors' Choice— Quantifying the Impact of Charge Transport Bottlenecks in Composite Cathodes of All-Solid-State Batteries. *J. Electrochem. Soc.* 2021, 168, No. 040537. https://doi.org/10.1149/1945-7111/abf8d7.
- (6) Kato, Y.; Shiotani, S.; Morita, K.; Suzuki, K.; Hirayama, M.; Kanno, R. All-Solid-State Batteries with Thick Electrode Configurations. *J. Phys. Chem. Lett.* **2018**, *9* (3), 607–613. https://doi.org/10.1021/acs.jpclett.7b02880.
- (7) Bielefeld, A.; Weber, D. A.; Janek, J. Modeling Effective Ionic Conductivity and Binder Influence in Composite Cathodes for All-Solid-State Batteries. *ACS Appl. Mater. Interfaces* **2020**, *12*, 12821–12833. https://doi.org/10.1021/acsami.9b22788.
- (8) Ohno, S.; Banik, A.; Dewald, G. F.; Kraft, M. A.; Krauskopf, T.; Minafra, N.; Till, P.; Weiss, M.; Zeier, W. G. Materials Design of Ionic Conductors for Solid State Batteries. *Progress in Energy* 2020, 2 (2), 022001. https://doi.org/10.1088/2516-1083/ab73dd.

- (9) Zhou, L.; Minafra, N.; Zeier, W. G.; Nazar, L. F. Innovative Approaches to Li-Argyrodite Solid Electrolytes for All-Solid-State Lithium Batteries. *Acc. Chem. Res.* 2021, 54, 2717– 2728. https://doi.org/10.1021/acs.accounts.0c00874.
- (10) Deiseroth, H. J.; Maier, J.; Weichert, K.; Nickel, V.; Kong, S. T.; Reiner, C. Li₇PS₆ and Li₆PS₅X (X: Cl, Br, I): Possible Three-Dimensional Diffusion Pathways for Lithium Ions and Temperature Dependence of the Ionic Conductivity by Impedance Measurements. *Z. Anorg. Allg. Chem.* **2011**, *637*, 1287–1294. https://doi.org/10.1002/zaac.201100158.
- (11) Zhou, L.; Assoud, A.; Zhang, Q.; Wu, X.; Nazar, L. F. New Family of Argyrodite Thioantimonate Lithium Superionic Conductors. *J. Am. Chem. Soc.* **2019**, *141*, 19002–19013. https://doi.org/10.1021/jacs.9b08357.
- (12) Kraft, M. A.; Ohno, S.; Zinkevich, T.; Koerver, R.; Culver, S. P.; Fuchs, T.; Senyshyn, A.; Indris, S.; Morgan, B. J.; Zeier, W. G. Inducing High Ionic Conductivity in the Lithium Superionic Argyrodites Li_{6+x}P_{1-x}Ge_xS₅I for All-Solid-State Batteries. *J. Am. Chem. Soc.* **2018**, *140*, 16330–16339. https://doi.org/10.1021/jacs.8b10282.
- (13) Hogrefe, K.; Minafra, N.; Hanghofer, I.; Banik, A.; Zeier, W. G.; Wilkening, H. M. R. Opening Diffusion Pathways through Site Disorder: The Interplay of Local Structure and Ion Dynamics in the Solid Electrolyte Li_{6+x}P_{1-x}Ge_xS₅I as Probed by Neutron Diffraction and NMR. *J. Am. Chem. Soc.* **2022**, *144*, 1795–1812. https://doi.org/10.1021/jacs.1c11571.
- (14) Ohno, S.; Helm, B.; Fuchs, T.; Dewald, G.; Kraft, M. A.; Culver, S. P.; Senyshyn, A.; Zeier, W. G. Further Evidence for Energy Landscape Flattening in the Superionic Argyrodites Li_{6+x}P_{1-x}M_xS₅I (M = Si, Ge, Sn). *Chem. Mater.* 2019, 31, 4936–4944. https://doi.org/10.1021/acs.chemmater.9b01857.
- (15) Hartel, J.; Banik, A.; Gerdes, J. M.; Wankmiller, B.; Helm, B.; Li, C.; Kraft, M. A.; Hansen, M. R.; Zeier, W. G. Understanding Lithium-Ion Transport in Selenophosphate-Based Lithium Argyrodites and Their Limitations in Solid-State Batteries. *Chem. Mater.* 2023, 35 (12), 4798–4809. https://doi.org/10.1021/acs.chemmater.3c00658.
- (16) Bernges, T.; Culver, S. P.; Minafra, N.; Koerver, R.; Zeier, W. G. Competing Structural Influences in the Li Superionic Conducting Argyrodites $Li_6PS_{5-x}Se_xBr$ ($0 \le x \le 1$) upon Se

- Substitution. *Inorg. Chem.* **2018**, *57*, 13920–13928. https://doi.org/10.1021/acs.inorgchem.8b02443.
- (17) Adeli, P.; Bazak, J. D.; Park, K. H.; Kochetkov, I.; Huq, A.; Goward, G. R.; Nazar, L. F. Boosting Solid-State Diffusivity and Conductivity in Lithium Superionic Argyrodites by Halide Substitution. *Angew. Chem. Int. Ed.* **2019**, *58*, 8681–8686. https://doi.org/10.1002/anie.201814222.
- (18) Gautam, A.; Ghidiu, M.; Suard, E.; Kraft, M. A.; Zeier, W. G. On the Lithium Distribution in Halide Superionic Argyrodites by Halide Incorporation in Li_{7-x}PS_{6-x}Cl_x. *ACS Appl. Energy Mater.* **2021**, *4*, 7309–7315. https://doi.org/10.1021/acsaem.1c01417.
- (19) Wang, P.; Liu, H.; Patel, S.; Feng, X.; Chien, P. H.; Wang, Y.; Hu, Y. Y. Fast Ion Conduction and Its Origin in Li_{6-x}PS_{5-x}Br_{1+x}. *Chem. Mater.* **2020**, *32*, 3833–3840. https://doi.org/10.1021/acs.chemmater.9b05331.
- (20) Lin, J.; Cherkashinin, G.; Schäfer, M.; Melinte, G.; Indris, S.; Kondrakov, A.; Janek, J.; Brezesinski, T.; Strauss, F. A High-Entropy Multicationic Substituted Lithium Argyrodite Superionic Solid Electrolyte. ACS Mater. Lett. 2022, 2187–2194. https://doi.org/10.1021/acsmaterialslett.2c00667.
- (21) Deiseroth, H. J.; Kong, S. T.; Eckert, H.; Vannahme, J.; Reiner, C.; Zaiß, T.; Schlosser, M. Li₆PS₅X: A Class of Crystalline Li-Rich Solids with an Unusually High Li⁺ Mobility. *Angew. Chem. Int. Ed.* **2008**, *47*, 755–758. https://doi.org/10.1002/anie.200703900.
- (22) Kraft, M. A.; Culver, S. P.; Calderon, M.; Böcher, F.; Krauskopf, T.; Senyshyn, A.; Dietrich, C.; Zevalkink, A.; Janek, J.; Zeier, W. G. Influence of Lattice Polarizability on the Ionic Conductivity in the Lithium Superionic Argyrodites Li₆PS₅X (X = Cl, Br, I). *J. Am. Chem. Soc.* 2017, 139, 10909–10918. https://doi.org/10.1021/jacs.7b06327.
- (23) Minafra, N.; Kraft, M. A.; Bernges, T.; Li, C.; Schlem, R.; Morgan, B. J.; Zeier, W. G. Local Charge Inhomogeneity and Lithium Distribution in the Superionic Argyrodites Li₆PS₅X (X = Cl, Br, I). *Inorg. Chem.* **2020**, *59*, 11009–11019. https://doi.org/10.1021/acs.inorgchem.0c01504.
- (24) De Klerk, N. J. J.; Rosłoń, I.; Wagemaker, M. Diffusion Mechanism of Li Argyrodite Solid Electrolytes for Li-Ion Batteries and Prediction of Optimized Halogen Doping: The Effect

- of Li Vacancies, Halogens, and Halogen Disorder. *Chem. Mater.* **2016**, *28*, 7955–7963. https://doi.org/10.1021/acs.chemmater.6b03630.
- (25) Morgan, B. J. Mechanistic Origin of Superionic Lithium Diffusion in Anion-Disordered Li₆PS₅X Argyrodites. *Chem. Mater.* **2021**, *33*, 2004–2018. https://doi.org/10.1021/acs.chemmater.0c03738.
- (26) Gautam, A.; Al-Kutubi, H.; Famprikis, T.; Ganapathy, S.; Wagemaker, M. Exploring the Relationship Between Halide Substitution, Structural Disorder, and Lithium Distribution in Lithium Argyrodites (Li_{6-x}PS_{5-x}Br_{1+x}). *Chem. Mater.* **2023**. https://doi.org/10.1021/acs.chemmater.3c01525.
- (27) Gautam, A.; Sadowski, M.; Ghidiu, M.; Minafra, N.; Senyshyn, A.; Albe, K.; Zeier, W. G. Engineering the Site-Disorder and Lithium Distribution in the Lithium Superionic Argyrodite Li₆PS₅Br. *Adv. Energy Mater.* **2021**, *11*. https://doi.org/10.1002/aenm.202003369.
- (28) Gautam, A.; Sadowski, M.; Prinz, N.; Eickhoff, H.; Minafra, N.; Ghidiu, M.; Culver, S. P.; Albe, K.; Fässler, T. F.; Zobel, M.; Zeier, W. G. Rapid Crystallization and Kinetic Freezing of Site-Disorder in the Lithium Superionic Argyrodite Li₆PS₅Br. *Chem. Mater.* **2019**, *31*, 10178−10185. https://doi.org/10.1021/acs.chemmater.9b03852.
- (29) Walther, F.; Koerver, R.; Fuchs, T.; Ohno, S.; Sann, J.; Rohnke, M.; Zeier, W. G.; Janek, J. Visualization of the Interfacial Decomposition of Composite Cathodes in Argyrodite-Based All-Solid-State Batteries Using Time-of-Flight Secondary-Ion Mass Spectrometry. Chem. Mater. 2019, 31, 3745–3755. https://doi.org/10.1021/acs.chemmater.9b00770.
- (30) Koerver, R.; Walther, F.; Aygün, I.; Sann, J.; Dietrich, C.; Zeier, W. G.; Janek, J. Redox-Active Cathode Interphases in Solid-State Batteries. *J. Mater. Chem. A Mater.* **2017**, *5* (43), 22750–22760. https://doi.org/10.1039/c7ta07641j.
- (31) Dewald, G. F.; Ohno, S.; Kraft, M. A.; Koerver, R.; Till, P.; Vargas-Barbosa, N. M.; Janek, J.; Zeier, W. G. Experimental Assessment of the Practical Oxidative Stability of Lithium Thiophosphate Solid Electrolytes. *Chem. Mater.* 2019, 31 (20), 8328–8337. https://doi.org/10.1021/acs.chemmater.9b01550.

- (32) Tan, D. H. S.; Wu, E. A.; Nguyen, H.; Chen, Z.; Marple, M. A. T.; Doux, J. M.; Wang, X.; Yang, H.; Banerjee, A.; Meng, Y. S. Elucidating Reversible Electrochemical Redox of Li₆PS₅Cl Solid Electrolyte. *ACS Energy Lett.* **2019**, 2418–2427. https://doi.org/10.1021/acsenergylett.9b01693.
- (33) Wang, S.; Tang, M.; Zhang, Q.; Li, B.; Ohno, S.; Walther, F.; Pan, R.; Xu, X.; Xin, C.; Zhang, W.; Li, L.; Shen, Y.; Richter, F. H.; Janek, J.; Nan, C. W. Lithium Argyrodite as Solid Electrolyte and Cathode Precursor for Solid-State Batteries with Long Cycle Life. Adv. Energy Mater. 2021, 11 (31), 1–10. https://doi.org/10.1002/aenm.202101370.
- (34) Zuo, T. T.; Rueß, R.; Pan, R.; Walther, F.; Rohnke, M.; Hori, S.; Kanno, R.; Schröder, D.; Janek, J. A Mechanistic Investigation of the Li₁₀GeP₂S₁₂|LiNi_{1-x-y}Co_xMn_yO₂ Interface Stability in All-Solid-State Lithium Batteries. *Nat. Commun.* **2021**, *12* (1), 6669. https://doi.org/10.1038/s41467-021-26895-4.
- (35) Strauss, F.; Teo, J. H.; Maibach, J.; Kim, A. Y.; Mazilkin, A.; Janek, J.; Brezesinski, T. Li₂ZrO₃-Coated NCM622 for Application in Inorganic Solid-State Batteries: Role of Surface Carbonates in the Cycling Performance. *ACS Appl. Mater. Interfaces* **2020**, *12* (51), 57146–57154. https://doi.org/10.1021/acsami.0c18590.
- (36) Jung, S. H.; Kim, U. H.; Kim, J. H.; Jun, S.; Yoon, C. S.; Jung, Y. S.; Sun, Y. K. Ni-Rich Layered Cathode Materials with Electrochemo-Mechanically Compliant Microstructures for All-Solid-State Li Batteries. *Adv. Energy Mater.* **2020**, *10* (6), 1–12. https://doi.org/10.1002/aenm.201903360.
- (37) Culver, S. P.; Koerver, R.; Zeier, W. G.; Janek, J. On the Functionality of Coatings for Cathode Active Materials in Thiophosphate-Based All-Solid-State Batteries. *Adv. Energy Mater.* **2019**, *9* (24), 1–14. https://doi.org/10.1002/aenm.201900626.
- (38) Walther, F.; Strauss, F.; Wu, X.; Mogwitz, B.; Hertle, J.; Sann, J.; Rohnke, M.; Brezesinski, T.; Janek, J. The Working Principle of a Li₂CO₃/LiNbO₃ Coating on NCM for Thiophosphate-Based All-Solid-State Batteries. *Chem. Mater.* 2021, 33 (6), 2110–2125. https://doi.org/10.1021/acs.chemmater.0c04660.
- (39) Herzog, M. J.; Esken, D.; Janek, J. Improved Cycling Performance of High-Nickel NMC by Dry Powder Coating with Nanostructured Fumed Al₂O₃, TiO₂, and ZrO₂: A Comparison. *Batter. Supercaps* **2021**, *4* (6), 1003–1017. https://doi.org/10.1002/batt.202100016.

- (40) Zuo, T. T.; Walther, F.; Ahmed, S.; Rueß, R.; Hertle, J.; Mogwitz, B.; Volz, K.; Janek, J. Formation of an Artificial Cathode-Electrolyte Interphase to Suppress Interfacial Degradation of Ni-Rich Cathode Active Material with Sulfide Electrolytes for Solid-State Batteries. ACS Energy Lett. 2023, 8 (3), 1322–1329. https://doi.org/10.1021/acsenergylett.2c02835.
- (41) Zuo, T. T.; Walther, F.; Teo, J. H.; Rueß, R.; Wang, Y.; Rohnke, M.; Schröder, D.; Nazar, L. F.; Janek, J. Impact of the Chlorination of Lithium Argyrodites on the Electrolyte/Cathode Interface in Solid-State Batteries. *Angewandte Chemie International Edition* 2022, 202213228. https://doi.org/10.1002/anie.202213228.
- (42) Chen, T.; Zhang, L.; Zhang, Z.; Li, P.; Wang, H.; Yu, C.; Yan, X.; Wang, L.; Xu, B. Argyrodite Solid Electrolyte with a Stable Interface and Superior Dendrite Suppression Capability Realized by ZnO Co-Doping. *ACS Appl. Mater. Interfaces* **2019**, *11* (43), 40808-40816. https://doi.org/10.1021/acsami.9b13313.
- (43) Schneider, H.; Sedlmaier, S. J.; Du, H.; Kelley, T.; Leitner, K.; ter Maat, J.; Schneider, L. Stabilization of Highly Conductive Lithium Argyrodites by Means of Lithium Substitution: the Case of Li₆Fe_{0.5}PS₆. *ChemistrySelect* **2019**, *4* (12), 3351-3354. https://doi.org/10.1002/slct.201803388.
- (44) Jiang, Z.; Liu, Y.; Peng, H.; Li, J.; Xu, X.; Su, H.; Tu, J. Enhanced Air Stability and Interfacial Compatibility of Li-Argyrodite Sulfide Electrolyte Triggered by CuBr Co-Substitution for All-Solid-State Lithium Batteries. *Energy Storage Materials* **2023**, *56*, 300-309. https://doi.org/10.1016/j.ensm.2023.01.018.
- (45) Choi, H.; Cho, S.; Kim, Y. S.; Cho, J. S.; Kim, H.; Lee, H.; Ko, S.; Kim, K.; Lee, S. M.; Hong, S. T.; Choi, C. H.; Seo, D. H.; Park, S. An Effective Catholyte for Sulfide-Based All-Solid-State Batteries Utilizing Gas Absorbents. *Small* 2024, 2403147. https://doi.org/10.1002/smll.202403147.
- (46) Li, S.; Wei, X.; Zhu, S.; Gui, Y. First Principles Analysis of SO2, H2S Adsorbed on Fe-ZnS Surface. Sens Actuators A Phys 2021, 329, 112827. https://doi.org/10.1016/j.sna.2021.112827.

- (47) Dewald, G. F.; Liaqat, Z.; Lange, M. A.; Tremel, W.; Zeier, W. G. Influence of Iron Sulfide Nanoparticle Sizes in Solid-State Batteries. *Angewandte Chemie* 2021, 133 (33), 18096– 18100. https://doi.org/10.1002/ange.202106018.
- (48) Coelho, A. A. TOPAS-Academic. Coelho Software: Brisbane, Australia 2007.
- (49) Zhang, W.; Weber, D. A.; Weigand, H.; Arlt, T.; Manke, I.; Schröder, D.; Koerver, R.; Leichtweiss, T.; Hartmann, P.; Zeier, W. G.; Janek, J. Interfacial Processes and Influence of Composite Cathode Microstructure Controlling the Performance of All-Solid-State Lithium Batteries. ACS Appl. Mater. Interfaces 2017, 9, 17835–17845. https://doi.org/10.1021/acsami.7b01137.
- (50) Santhosha, A. L.; Medenbach, L.; Buchheim, J. R.; Adelhelm, P. The Indium–Lithium Electrode in Solid-State Lithium-Ion Batteries: Phase Formation, Redox Potentials, and Interface Stability. *Batter. Supercaps* 2019, 2 (6), 524–529. https://doi.org/10.1002/batt.201800149.
- (51) Shannon, R. D.; Prewitt, C. T. Revised Values of Effective Ionic Radii. *Acta Crystallogr. B*1970, 26, 1046–1048. https://doi.org/10.1107/S0567740870003576.
- (52) Denton, A. R.; Ashcroft, N. W. Vegard's Law. Phys. Rev. A 1991, 43 (6), 3161.
- (53) Irvine, J. T. S.; Sinclair, D. C.; West, A. R. Electroceramics: Characterization by Impedance Spectroscopy. *Adv. Mater.* **1990**, *2*, 132–138. https://doi.org/10.1002/adma.19900020304.
- (54) Ohno, S.; Bernges, T.; Buchheim, J.; Duchardt, M.; Hatz, A. K.; Kraft, M. A.; Kwak, H.; Santhosha, A. L.; Liu, Z.; Minafra, N.; Tsuji, F.; Sakuda, A.; Schlem, R.; Xiong, S.; Zhang, Z.; Adelhelm, P.; Chen, H.; Hayashi, A.; Jung, Y. S.; Lotsch, B. V.; Roling, B.; Vargas-Barbosa, N. M.; Zeier, W. G. How Certain Are the Reported Ionic Conductivities of Thiophosphate-Based Solid Electrolytes? An Interlaboratory Study. ACS Energy Lett. 2020, 5, 910–915. https://doi.org/10.1021/acsenergylett.9b02764.
- Rosenbach, C.; Walther, F.; Ruhl, J.; Hartmann, M.; Hendriks, T. A.; Ohno, S.; Zeier, W.
 G. Visualizing the Chemical Incompatibility of Halide and Sulfide-Based Electrolytes in Solid-State Batteries. *Adv. Energy Mater.* 2023, *13*(6), 2203673. https://doi.org/10.1002/aenm.202203673.

- (56) Koerver, R.; Aygün, I.; Leichtweiß, T.; Dietrich, C.; Zhang, W.; Binder, J. O.; Hartmann, P.; Zeier, W. G.; Janek, J. Capacity Fade in Solid-State Batteries: Interphase Formation and Chemomechanical Processes in Nickel-Rich Layered Oxide Cathodes and Lithium Thiophosphate Solid Electrolytes. *Chem. Mater.* 2017, 29 (13), 5574–5582. https://doi.org/10.1021/acs.chemmater.7b00931.
- (57) de Biasi, L.; Schwarz, B.; Brezesinski, T.; Hartmann, P.; Janek, J.; Ehrenberg, H. Chemical, Structural, and Electronic Aspects of Formation and Degradation Behavior on Different Length Scales of Ni-Rich NCM and Li-Rich HE-NCM Cathode Materials in Li-Ion Batteries. *Adv. Mater.* **2019**, *31* (26), 1900985. https://doi.org/10.1002/adma.201900985.
- (58) Walther, F.; Randau, S.; Schneider, Y.; Sann, J.; Rohnke, M.; Richter, F. H.; Zeier, W. G.; Janek, J. Influence of Carbon Additives on the Decomposition Pathways in Cathodes of Lithium Thiophosphate-Based All-Solid-State Batteries. *Chem. Mater.* **2020**, *32* (14), 6123–6136. https://doi.org/10.1021/acs.chemmater.0c01825.
- (59) Zhang, W.; Weber, D. A.; Weigand, H.; Arlt, T.; Manke, I.; Schröder, D.; Koerver, R.; Leichtweiss, T.; Hartmann, P.; Zeier, W. G. Interfacial Processes and Influence of Composite Cathode Microstructure Controlling the Performance of All-Solid-State Lithium Batteries. ACS Appl. Mater. Interfaces 2017, 9 (21), 17835–17845. https://doi.org/10.1021/acsami.7b01137.
- (60) Ruhl, J.; Riegger, L. M.; Ghidiu, M.; Zeier, W. G. Impact of Solvent Treatment of the Superionic Argyrodite Li₆PS₅Cl on Solid-State Battery Performance. *Advanced Energy and Sustainability Research* **2021**, *2* (2), 2000077. https://doi.org/10.1002/aesr.202000077.
- (61) Banik, A.; Liu, Y.; Ohno, S.; Rudel, Y.; Jiménez-Solano, A.; Gloskovskii, A.; Vargas-Barbosa, N. M.; Mo, Y.; Zeier, W. G. Can Substitutions Affect the Oxidative Stability of Lithium Argyrodite Solid Electrolytes? *ACS Appl. Energy Mater.* **2022**, *5*, 2045–2053. https://doi.org/10.1021/acsaem.1c03599.
- (62) Wenzel, S.; Randau, S.; Leichtweiß, T.; Weber, D. A.; Sann, J.; Zeier, W. G.; Janek, J. Direct Observation of the Interfacial Instability of the Fast Ionic Conductor Li₁₀GeP₂S₁₂ at the

- Lithium Metal Anode. *Chemistry of Materials* **2016**, *28* (7), 2400–2407. https://doi.org/10.1021/acs.chemmater.6b00610.
- (63) Korte, C.; Ravishankar, N.; Carter, C. B.; Schmalzried, H. Kinetics of Spinel Formation in an External Applied Electric Field. *Solid State Ion.* **2002**, *148* (1–2), 111–121. https://doi.org/10.1016/S0167-2738(02)00101-7.
- (64) Auvergniot, J.; Cassel, A.; Foix, D.; Viallet, V.; Seznec, V.; Dedryvère, R. Redox Activity of Argyrodite Li₆PS₅Cl Electrolyte in All-Solid-State Li-Ion Battery: An XPS Study. *Solid State Ion.* **2017**, *300*, 78–85. https://doi.org/10.1016/j.ssi.2016.11.029.
- (65) Auvergniot, J.; Cassel, A.; Ledeuil, J.-B.; Viallet, V.; Seznec, V.; Dedryvère, R. Interface Stability of Argyrodite Li₆PS₅Cl toward LiCoO₂, LiNi_{1/3}Co_{1/3}Mn_{1/3}O₂, and LiMn₂O₄ in Bulk All-Solid-State Batteries. *Chem. Mater.* **2017**, *29* (9), 3883–3890. https://doi.org/10.1021/acs.chemmater.6b04990.
- (66) Naumkin, A. V.; Kraut-Vass, A.; Gaarenstroom, S. W.; Powell, C. J. *NIST X-ray Photoelectron Spectroscopy Database (SRD 20), Version 5.0.* https://srdata.nist.gov/xps/ (accessed 2024-05-02).
- (67) Appapillai, A. T.; Mansour, A. N.; Cho, J.; Shao-Horn, Y. Microstructure of LiCoO₂ with and without "AlPO₄" Nanoparticle Coating: Combined STEM and XPS Studies. *Chem. Mater.* **2007**, *19* (23), 5748–5757. https://doi.org/10.1021/cm0715390.
- (68) Nagao, K.; Hayashi, A.; Deguchi, M.; Tsukasaki, H.; Mori, S.; Tatsumisago, M. Amorphous LiCoO₂-Li₂SO₄ Active Materials: Potential Positive Electrodes for Bulk-Type All-Oxide Solid-State Lithium Batteries with High Energy Density. *J. Power Sources* **2017**, *348*, 1–8. https://doi.org/10.1016/j.jpowsour.2017.02.038.
- (69) Jung, R.; Metzger, M.; Maglia, F.; Stinner, C.; Gasteiger, H. A. Oxygen Release and Its Effect on the Cycling Stability of LiNi_xMn_yCo_zO₂ (NMC) Cathode Materials for Li-Ion Batteries. *J. Electrochem. Soc.* **2017**, *164* (7), A1361. https://doi.org/10.1149/2.0021707jes.
- (70) Strauss, F.; Teo, J. H.; Schiele, A.; Bartsch, T.; Hatsukade, T.; Hartmann, P.; Janek, J.; Brezesinski, T. Gas Evolution in Lithium-Ion Batteries: Solid versus Liquid Electrolyte.

ACS Appl. Mater. Interfaces **2020**, 12 (18), 20462–20468. https://doi.org/10.1021/acsami.0c02872.

For table of contents only

CEI design?

